CERN-LPCC-2018-XX

Dark Matter Working Group: Draft of the 2HDM+a whitepaper

Authors missing!

Abstract. Let's play the music and not the background!

Contents

1 Introduction

[Uli: Still have to go through the text below!]

Dark matter (DM) is one of the main search targets for LHC [?] experiments (for a recent review, see e.g. Ref. [?]).

Based on the characteristics of DM as a weakly interacting massive particle (WIMP) [?], the ATLAS [?] and CMS [?] experiments at the LHC have searched for DM particle candidates manifesting as particles that escape the detectors in the form of missing transverse momentum ($E_T^{\rm miss}$). The design of experimental searches for invisible particles can in principle be kept independent from specific theoretical models, reflecting the lack of hints on the exact particle nature of DM. However, theoretical benchmarks are necessary to sharpen the search sensitivity, to characterize a possible discovery and to define a theoretical framework for comparison with non-collider results.

Supersymmetry has been the theoretical framework used as a benchmark for many particle dark matter searches at the LHC. Non-supersymmetric LHC search benchmarks evolved with time: at the start of data taking, Effective Field Theories (EFT) were used due to their relative model independence [? ? ? ? ? ?]. Further developments towards simplified models, each representing simple, single processes encapsulating the phenomenology of LHC DM interactions using a small set of parameters, occurred towards the start of the second LHC run [?]. The coherent adoption of these simplified models by the LHC collaborations focused the LHC DM experimental search program, especially in the presentation of its results and their comparison to direct detection (DD) and indirect detection (ID) [? ? ? ?]. Throughout this time, the community has been aware of the shortcomings related to the simplicity of these benchmark models, in particular the lack of theoretical consistency at all scales for some of them [? ? ? ?] and their limited phenomenology leading to the relevance of only a small set of experimental signatures.

With this whitepaper, we take a step beyond these simplified models by identifying an example benchmark model and its parameters to be tested by LHC searches, with the following characteristics:

- the model should preferably be an extension of one of one of the simplified models already used by the experimental collaborations;
- the model should still be generic enough to be used in the context of broader, more complete theoretical frameworks.
- the model should be gauge invariant;
- the model should have a sufficiently varied phenomenology to encourage comparison of different experimental signatures and search for DM in new, unexplored signatures;
- the model should be of interest beyond the DM community, so that it can link to existing efforts and that other direct and indirect constraints can be identified;

The model chosen in this whitepaper is a Two-Higgs-Doublet-Model (2HDM) [?] [asked Higgs BSM people] with the addition of a pseudoscalar boson mediating the interaction between DM and SM, termed 2HDM+a in the following. It is the simplest renormalisable extension of a 2HDM and includes a SM-singlet DM candidate [? ? ? ? ?]. It adds an extended scalar sector to the pseudoscalar model in [? ?], and is gauge invariant. The first section of this whitepaper (section 2) describes the evolution of theories for LHC DM searches and details the characteristics of this model. It also provides guidance on the choice of benchmark parameters to be used by LHC searches, from considerations of vacuum stability consideration.

In ??, we investigate in detail the kinematic distributions of this model for three experimental signatures that are sensitive to this model:

- the Higgs+E_T^{miss} signature, where the E_T^{miss} is produced by the decay of the pseudoscalar that couples to dark matter and the Higgs is produced either in association with this pseudoscalar or as a product of the decay of the second pseudoscalar;
- the Z+E_T^{miss} signature, where the E_T^{miss} is produced by the decay of the pseudoscalar that couples to dark matter and the Z boson is either produced in association with this pseudoscalar or radiated by the heavy Higgs boson;
- the $t\bar{t}$+E_T^{miss} signature, where pseudoscalar that couples to dark matter is produced in association with a $t\bar{t}$ pair or radiated by one of the top quarks. Notably, the kinematic distributions of the simplified pseudoscalar model can be rescaled to correspond to the 2HDM+a.

The variation of the kinematic distributions with the parameters of the model is a useful indicator of the generality of the search strategy with respect to the specific choices of model parameters that will be adopted by the collaborations.

The sensitivity of searches for this model in those signatures, determined at generator-level in ??, surpasses that of the jet+E_T^{miss} searches, providing a motivation to explore their parameter space beyond the $s-$channel simplified models in [?]. Moreover, we identify a number of other existing and unexplored signatures that are sensitive to this model and can be studied using dedicated searches in the future.

Finally, we investigate the connection of this model with the relic abundance of DM in the universe in section 10, and sketch the path forward to determine the complementarity of collider searches with DD and ID searches in ??.

2 Evolution of theories for LHC DM searches

The experimental results of two of the three DM search strategies, namely direct and indirect detection, are commonly interpreted in the DM effective field theory (DM-EFT) framework. The operators in these DM-EFTs are build from SM fermions and DM fields. Schematically, one has in the case of spin-0 interactions and Dirac fermion DM

$$\mathcal{L}_{\text{DM-EFT}} = \sum_{f=u,d,\ell} \left(\frac{C_1^f}{\Lambda^2} \bar{f} f \bar{\chi}\chi + \frac{C_2^f}{\Lambda^2} \bar{f}\gamma_5 f \bar{\chi}\gamma_5\chi + \dots \right) , \tag{2.1}$$

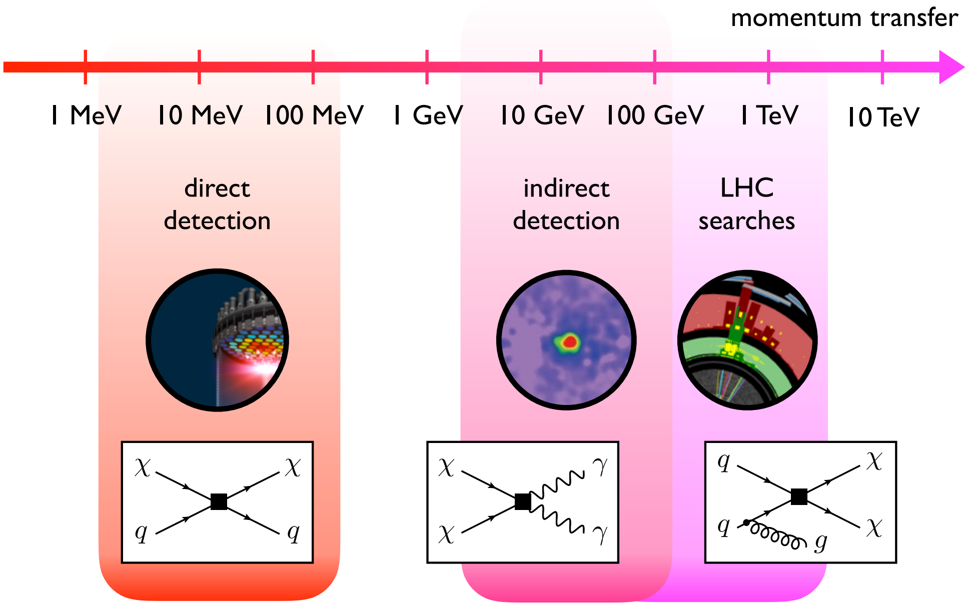

Figure 1: Range of momenta probed in direct-detection experiments, indirect-detection experiments and LHC searches. Prototypes of relevant Feynman diagrams are also shown.

where the ellipsis represents additional operators not relevant for the further discussion, the sum over $f = u, d, \ell$ includes all SM quarks and leptons, the DM candidate is called χ and γ_5 denotes the fifth Dirac matrix. The above DM-EFT is fully described by the parameters

$$\{m_\chi\,,\ C_n^f/\Lambda^2\}\,. \tag{2.2}$$

Here m_χ is the mass of the DM candidate, Λ is the suppression scale of the higher-dimensional operators and the C_n^f are the so-called Wilson coefficients. Notice that Λ and C_n^f are not independent parameters but always appear in the specific combination given in (2.2).

The DM-EFT approach is justified for the small momentum transfer $q^2 \ll \Lambda^2$ in DM-nucleon scattering (set by the non-relativistic velocities of DM in the halo) and in DM annihilation (set by the mass of the annihilating DM candidate). See Figure 1 for an illustration of the relevant scales in each experiment. Early articles [**? ? ? ? ? ?**] on DM searches at colliders quantify the reach of the LHC in the parameter space in terms of (2.2) and similar operators. The momentum transfer at the LHC is however larger than the suppression scale, i.e. $q^2 \gg \Lambda^2$, for many theories of DM. In this case, the mediator of the interaction between the dark sector and the SM can be resonantly produced and predictions obtained using the DM-EFT framework often turn out to be inaccurate (see for instance [**? ? ? ? ? ? ? ? ?**] and [**? ?**] for exceptions).

The kinematics of on-shell propagators can be captured in DM simplified models, which aim to represent a large number of extensions of the SM, while keeping only the degrees of freedom relevant for LHC phenomenology [**? ?**]. In the case of a pseudoscalar mediator a, the relevant DM-mediator and SM-mediator interactions read

$$\mathcal{L}_{\text{DM-SIMP}} = -ig_\chi a \bar{\chi}\gamma_5\chi - ia\sum_j \left(g_u y_j^u \bar{u}_j \gamma_5 u_j + g_d y_j^d \bar{d}_j \gamma_5 d_j + g_\ell y_j^\ell \bar{\ell}_j \gamma_5 \ell_j \right) , \tag{2.3}$$

with j representing a flavour index. Since the mediator a is a singlet it can also couple to itself and to $H^\dagger H$ where H denotes the SM Higgs doublet. The most general renormalisable scalar potential for a massive a is therefore

$$V_{\text{DM-SIMP}} = \frac{1}{2} m_a^2 a^2 + b_a a^3 + \lambda_a a^4 + b_H a H^\dagger H + \lambda_H a^2 H^\dagger H \, . \tag{2.4}$$

The parameters b_H and λ_H determine the couplings between the a and the H fields, thereby altering both the interactions and CP properties of the SM-like scalar h at 125 GeV as well as giving rise to possible new decay channels such as $h \to aa$ (see [? ?] for details on the LHC phenomenology). Avoiding the resulting strong constraints for any choice of m_a, requires that $b_H \ll m_a$ and $\lambda_H \ll 1$. While the former requirement can be satisfied by imposing a Z_2 symmetry $a \to -a$, in the latter case one has to assume that λ_H is accidentally small if $m_a \lesssim 100\,\text{GeV}$ (cf. the related discussion on invisible decays of the Higgs boson in Section 4). Under such an assumption and noting that the self-coupling λ_a is largely irrelevant for collider phenomenology, the DM simplified model is fully described by the parameters

$$\left\{ m_\chi ,\; m_a \, ,\; g_\chi \, ,\; g_u \, ,\; g_d \, ,\; g_\ell \right\} . \tag{2.5}$$

In fact, in the limit of infinite mediator mass $m_a \to \infty$, the DM-SIMP Lagrangian (2.3) matches onto the DM-EFT Lagrangian (2.1). The corresponding tree-level matching conditions are $C_2^f/\Lambda^2 = g_\chi g_f y_f / m_a^2$ and $C_n^f = 0$ for all other Wilson coefficients.

Unfortunately, the operators in both $\mathcal{L}_{\text{DM-EFT}}$ and $\mathcal{L}_{\text{DM-SIMP}}$ violate gauge invariance, because the left- and right-handed SM fermions belong to different representations of the SM gauge group. In the case of the DM-EFT this suggests the Wilson coefficients C_n^f introduced in (2.1) actually scale as $C_n^f = c_n^f m_{f_i}/\Lambda$ [?], whereas for the DM simplified model restoring gauge invariance requires the embedding of the mediator a into an electroweak (EW) multiplet. The absence of gauge invariance leads to unitarity-violating amplitudes in DM simplified models (cf. [? ? ? ?]). In the case of the DM simplified model described by (2.3), one can show for instance that the amplitudes $\mathcal{A}(qb \to q'ta) \propto \sqrt{s}$ and $\mathcal{A}(gg \to Za) \propto \ln^2 s$ diverge in the limit of large center-of-mass energy s. The Feynman diagrams that lead to this behaviour are depicted on the left-hand side in Figure 2. Similar singularities appear in other single-top processes and in the mono-Higgs case. Since the divergences are not power-like, weakly-coupled realisations of (2.3) do not break down for the energies accessible at the LHC. The appearance of the $\sqrt{s}$ and $\ln^2 s$ terms however signals the omission of diagrams that would be present in any gauge-invariant extension that gives rise to $\mathcal{L}_{\text{DM-EFT}}$ in the limit where all additional particles are heavy. For example, the $pp \to tja$ cross section is made finite by the exchange of a charged Higgs $H^\pm$, while in the case of $pp \to Za$ an additional scalar H unitarises the amplitude. The corresponding

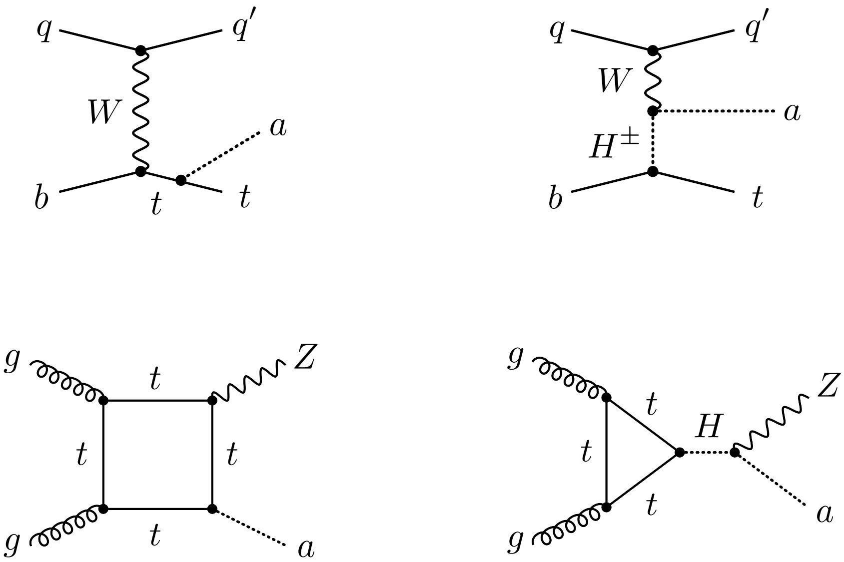

Figure 2: Diagrams contributing to the $qb \to q'ta$ (upper row) and $gg \to Za$ (lower row) scattering processes. Only the graphs on the left-hand side appear in the DM simplified model with a pseudoscalar, while in the 2HDM+a model in addition the diagrams on the right-hand side are present. See text for further details.

diagrams are displayed on the right in Figure 2. Notice that the cancellation of unitarity-violating terms among the diagrams of the latter figure is not at all accidental, but a direct consequence of the local gauge invariance of the underlying model.

The additional degrees of freedom necessary to unitarise the amplitudes cannot be arbitrarily heavy and hence may change the phenomenology of the DM simplified model. In fact, as can be seen from Figure 2, the presence of the $H^\pm$ (H) allows to produce a mono-top (mono-Z) signal resonantly. Since resonant production is strongly enhanced compared to initial state radiation, the importance of the various mono-X signals in the extended DM model may then differ from the simplified model predictions [**? ? ?**]. In fact, we will see that in a specific extension of (2.3) called 2HDM+a model, the mono-Higgs, mono-Z and $tX + E_T^{\rm miss}$ signals can be as or even more important than the $t\bar{t} + E_T^{\rm miss}$ and mono-jet channel, which are the leading missing transverse energy ($E_T^{\rm miss}$) signatures in the DM simplified pseudoscalar model [**? ? ? ? ?**]. We emphasise that the embedding of (2.3) is not unique, since both the mediator and the DM particle can belong to different EW multiplets. In this whitepaper, we consider the simplest embedding with a single SM-singlet DM candidate, which captures the maximal number of interesting $E_{T,\rm miss}$ signatures. We will briefly comment on other possible embeddings and related DM models in Section 5.

3 Description of the 2HDM+a model

The 2HDM+a model is a two Higgs doublet model (2HDM) that contains, besides the Higgs doublets H_1 and H_2, an additional pseudoscalar singlet P. It is the simplest renormalisable extension of (2.3) with a SM-singlet DM candidate [? ? ? ? ?]. The gauge symmetry is made manifest by coupling the P to the dark Dirac fermion χ via

$$\mathcal{L}_\chi = -iy_\chi P\bar{\chi}\gamma_5\chi\,, \tag{3.1}$$

while the Higgs doublets couple to the SM fermions through

$$\mathcal{L}_Y = -\sum_{i=1,2}\left(\bar{Q}Y_u^i\tilde{H}_i u_R + \bar{Q}Y_d^i H_i d_R + \bar{L}Y_\ell^i H_i \ell_R + \text{h.c.}\right)\,. \tag{3.2}$$

Here y_χ is a dark-sector Yukawa coupling, Y_f^i are Yukawa matrices acting on the three fermion generations and we have suppressed flavour indices, Q and L are left-handed quark and lepton doublets, while u_R, d_R and ℓ_R are right-handed up-type quark, down-type quark and charged lepton singlets, respectively. Finally, $\tilde{H}_i = \epsilon H_i^*$ with ϵ denoting the two-dimensional antisymmetric tensor.

The particle that mediates the interactions between the dark sector and the SM is a superposition of the CP-odd components of H_1, H_2 and P. We impose a Z_2 symmetry under which $H_1 \to H_1$ and $H_2 \to -H_2$, such that only one Higgs doublet appears in each operator in $\mathcal{L}_Y$. The different ways to construct these operators result in different Yukawa structures and in this whitepaper we will, for concreteness, consider only the so-called type-II 2HDM. This specific choice corresponds to setting $Y_u^1 = Y_d^2 = Y_\ell^2 = 0$ in (3.2). The Z_2 symmetry is the minimal condition necessary to guarantee the absence of flavour-changing neutral currents (FCNCs) at tree-level [? ?] and such a symmetry is realised in many well-motivated complete ultraviolet (UV) theories in the form of supersymmetry, a $U(1)$ symmetry or a discrete symmetry acting on the Higgs doublets. We further choose all parameters in the scalar potential real, such that CP eigenstates are identified with the mass eigenstates, i.e. two scalars h and H, two pseudoscalars A and a and a charged scalar $H^\pm$. Under these conditions, the most general renormalisable scalar potential can be written as

$$V = V_H + V_{HP} + V_P\,, \tag{3.3}$$

with the potential for the two Higgs doublets

$$\begin{aligned} V_H = {} & \mu_1 H_1^\dagger H_1 + \mu_2 H_2^\dagger H_2 + \left(\mu_3 H_1^\dagger H_2 + \text{h.c.}\right) + \lambda_1\left(H_1^\dagger H_1\right)^2 + \lambda_2\left(H_2^\dagger H_2\right)^2 \\ & + \lambda_3\left(H_1^\dagger H_1\right)\left(H_2^\dagger H_2\right) + \lambda_4\left(H_1^\dagger H_2\right)\left(H_2^\dagger H_1\right) + \left[\lambda_5\left(H_1^\dagger H_2\right)^2 + \text{h.c.}\right]\,, \end{aligned} \tag{3.4}$$

potential terms which connect doublets and singlets

$$V_{HP} = P\left(ib_P H_1^\dagger H_2 + \text{h.c.}\right) + P^2\left(\lambda_{P1} H_1^\dagger H_1 + \lambda_{P2} H_2^\dagger H_2\right)\,, \tag{3.5}$$

and the singlet potential

$$V_P = \frac{1}{2}m_P^2 P^2\,. \tag{3.6}$$

Notice that compared to [? ? ? ?] which include only the trilinear portal coupling b_P, we follow [?] and also allow for quartic portal interactions proportional to λ_{P1} and λ_{P1}.

A quartic self-coupling P^4 has instead not been included in (3.6), because such a term would not lead to any relevant effect in the $E_T^{\rm miss}$ observables studied in this whitepaper.

Upon rotation to the mass eigenbasis, we trade the five dimensionful and the eight dimensionless parameters in the potential for physical masses and mixing angles and four quartic couplings:

$$\left\{ \begin{array}{c} \mu_1,\, \mu_2,\, \mu_3,\, b_P,\, m_P,\, m_\chi \\ y_\chi,\, \lambda_1,\, \lambda_2,\, \lambda_3,\, \lambda_4,\, \lambda_5, \\ \lambda_{P1},\, \lambda_{P2} \end{array} \right\} \quad \longleftrightarrow \quad \left\{ \begin{array}{c} v,\, M_h,\, M_A,\, M_H,\, M_{H^\pm},\, M_a,\, m_\chi \\ \cos(\beta-\alpha),\, \tan\beta,\, \sin\theta, \\ y_\chi,\, \lambda_3,\, \lambda_{P1},\, \lambda_{P_2} \end{array} \right\} . \tag{3.7}$$

The parameters shown on the right-hand side of (3.7) will be used as input in the following. Out of these parameters, the EW vacuum expectation value (VEV) $v \simeq 246\,\text{GeV}$ and the mass of the SM-like CP-even mass eigenstate $M_h \simeq 125\,\text{GeV}$ are already fixed by observations. The experimental and theoretical constraints on the remaining parameter space will be examined in the next section.

4 Constraints on the 2HDM+a parameter space

In the following we examine the constraints on the input parameters (3.7) that arise from Higgs and flavour physics, LHC searches for additional Higgses, EW precision measurements and vacuum stability considerations. The discussed constraints will motivate certain parameter benchmarks. These will be summarised at the end of the section.

Constraints on $\cos(\beta - \alpha)$

The mixing angle α between the CP-even scalars h and H is constrained by Higgs coupling strength measurements and we display the regions in the $\cos(\beta-\alpha)-\tan\beta$ plane that are allowed by the LHC Run-I combination [?] in the left panel of Figure 3. The shown 95% confidence level (CL) contour has been obtained in the type-II 2HDM. One observes that for arbitrary values of $\tan\beta$ only parameter choices with $\cos(\beta-\alpha) \simeq 0$ are experimentally allowed. To avoid the constraints from Higgs physics and to simplify the further analysis, we will concentrate in this whitepaper on the so-called alignment limit of the 2HDM where $\cos(\beta-\alpha) = 0$ [?], treating $\tan\beta$ as a free parameter.

Constraints on $\tan\beta$

Indirect constraints on $\tan\beta$ as a function of $M_{H^\pm}$ arise from $B \to X_s\gamma$ [? ? ?], B-meson mixing [? ? ? ?] as well as $B_s \to \mu^+\mu^-$ [? ? ? ? ? ? ?], but also follow from $Z \to b\bar{b}$ [? ? ?]. For the case of the type-II 2HDM, the most stringent constraints on the $M_{H^\pm}-\tan\beta$ plane are depicted in the right panel of Figure 3. From the shown results it is evident that $B \to X_s\gamma$ provides a lower limit on the charged Higgs mass of $M_{H^\pm} > 580\,\text{GeV}$ that is practically independent of $\tan\beta$ for $\tan\beta \gtrsim 2$, while $B_s \to \mu^+\mu^-$ is the leading constraint for very heavy charged Higgses, excluding for instance values of $\tan\beta < 1.3$ for $M_{H^\pm} = 1\,\text{TeV}$. As discussed in Section 7, the constraints on $\tan\beta$ that follow from the existing LHC searches for heavy Higgses (see for instance [? ? ? ? ? ?])

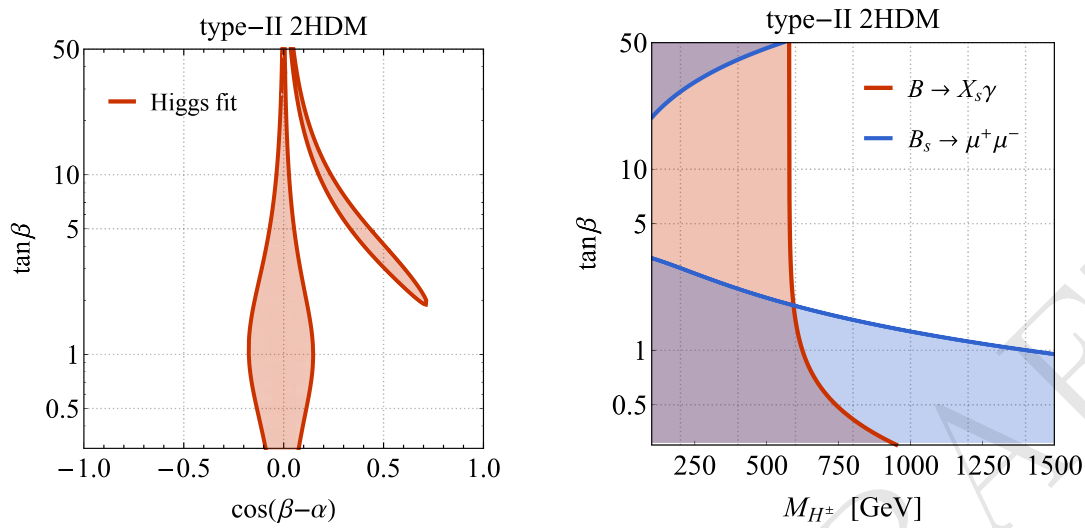

Figure 3: Left: Parameter space allowed by a global fit to the LHC Run-I Higgs coupling strength measurements. The lines show the contours which restrict the allowed parameter space at the 95% CL for a type-II 2HDM. Right: Parameter space in the $M_{H^\pm}-\tan\beta$ plane that is disfavoured by the flavour observables $B \to X_s\gamma$ (red) and $B_s \to \mu^+\mu^-$ (blue). The uncoloured region in the upper right corner of the plot is allowed at 95% CL.

are at the moment all weaker than the limits provided by flavour physics [?]. Since the indirect constraints arise from loop corrections they can in principle be weakened by the presence of additional particles that are too heavy to be produced at the LHC. We thus consider the bounds from flavour only as indicative, and will not directly impose them on the parameter space of the 2HDM+a in what follows.

Constraints on $\sin\theta$

EW precision measurements constrain the splittings between the masses $M_H, M_A, M_{H^\pm}$ and M_a, since the exchange of spin-0 states modifies the propagators of the W- and Z-bosons at the one-loop level and beyond. For $M_H = M_{H^\pm}$ and $\cos(\beta-\alpha) = 0$, these corrections vanish due to a custodial symmetry in the tree-level potential V_H [? ? ? ? ?] introduced in (3.4) and the masses of the CP-odd mass eigenstates can be treated as free parameters. This custodial symmetry is also present if $M_A = M_{H^\pm}$ and $\cos(\beta-\alpha) = 0$, but the presence of the pseudoscalar mixing term in (3.5) breaks this symmetry softly [?]. As a result, the pseudoscalar mixing angle θ and the mass splitting between M_H, M_A and M_a are constrained in such a case. An illustrative example of the resulting constraints is given in the left panel of Figure 4. To keep $\sin\theta$ and M_a as free parameters, we consider below only 2HDM+a model realisations in which the masses of the H, A and $H^\pm$ are equal. Notice that the choice $M_H = M_A = M_{H^\pm}$ is also adopted in some 2HDM interpretations of the searches for heavy spin-0 resonances performed at the LHC (cf. [? ? ?] for example).

Constraints on M_a

Invisible decays of the Higgs boson allow to set a lower limit on the mass of the pseudoscalar a in 2HDM+a scenarios with light DM [?]. In the case of $m_\chi = 1\,\text{GeV}$, it turns out for instance that mediator mass $M_a \lesssim 100\,\text{GeV}$ are excluded by imposing the 95% CL limit $\text{BR}(h \to \text{invisible}) \lesssim 25\%$ [? ?]. This limit is largely independent of the choices of the other parameters since $\text{BR}(h \to \text{invisible}) \simeq \text{BR}(h \to aa^* \to 2\chi 2\bar{\chi}) \simeq 100\%$ for sufficiently light DM. To evade the limits from invisible Higgs decays, we consider in this whitepaper only a masses larger than 100 GeV when studying E_T^{miss} signatures at the LHC.

Constraints on λ_3

The requirement that the scalar potential (3.3) of the 2HDM+a is bounded from below (BFB), restricts the possible choices of the Higgs masses, mixing angles and quartic couplings. Assuming that $\lambda_{P1}, \lambda_{P2} > 0$, it is easy to see that the BFB conditions in the 2HDM+a are identical to those found in the pure 2HDM [?]. For our choice $M_H = M_A = M_{H^\pm}$ of heavy Higgs masses, one finds that the tree-level BFB conditions can be cast into two inequalities. The first inequality connects λ_3 with the cubic SM Higgs self-coupling $\lambda = M_h^2/(2v^2) \simeq 0.13$ and simply reads

$$\lambda_3 > 2\lambda\,. \tag{4.1}$$

The second BFB condition relates λ_3 with $\tan\beta$, $\sin\theta$, the common heavy Higgs mass M_H and M_a and turns out to be more complicated. In the limit $M_H \gg M_h, M_a$ it however takes a rather simple form that we quote here for illustration:

$$\lambda_3 > \frac{M_H^2 - M_a^2}{v^2}\sin^2\theta - 2\lambda\cot^2(2\beta)\,. \tag{4.2}$$

This formula in essence implies that large values of $M_H^2/v^2 \sin^2\theta$ are only compatible with the requirements from BFB if the quartic coupling λ_3 is sufficiently large. Notice that the interplay between BFB and perturbativity of λ_3, i.e. $\lambda_3 < 4\pi$, leads to a non-decoupling of H, A and $H^\pm$ for $|M_H - M_a| \neq 0$ and $\sin\theta \neq 0$ [?] such that the spin-0 states are potentially within LHC reach. The right plot in Figure 4 which shows the constraints in the M_a–M_H plane that derive from the exact version of (4.2) puts the latter statement on solid ground. From the figure one observes that for $\tan\beta = 1$, $\sin\theta = 0.35$ and $M_H = M_A = M_{H^\pm}$, values of $\lambda_3 \gtrsim 2$ are needed in order for $M_H \simeq 1\,\text{TeV}$ to be allowed by BFB. Notice that due to the $\sin^2\theta$ dependence in (4.2), close to non-perturbative couplings $\lambda_3 \gtrsim 8$ would be required to make 1 TeV 2HDM Higgses viable for are larger pseudoscalar mixing angle of $\sin\theta = 0.7$. In order for heavy Higgs above 1 TeV to be acceptable while keeping λ_3 perturbative, we will choose $\sin\theta = 0.35$ and $\lambda_3 = 3$ as our benchmark in this whitepaper.

Constraints on λ_{P1} and λ_{P2}

The quartic couplings λ_3, λ_{P1} and λ_{P2} affect all cubic Higgs interactions. In the case of the Haa and Aah couplings, one obtains under the assumption that $\cos(\beta - \alpha) = 0$ and

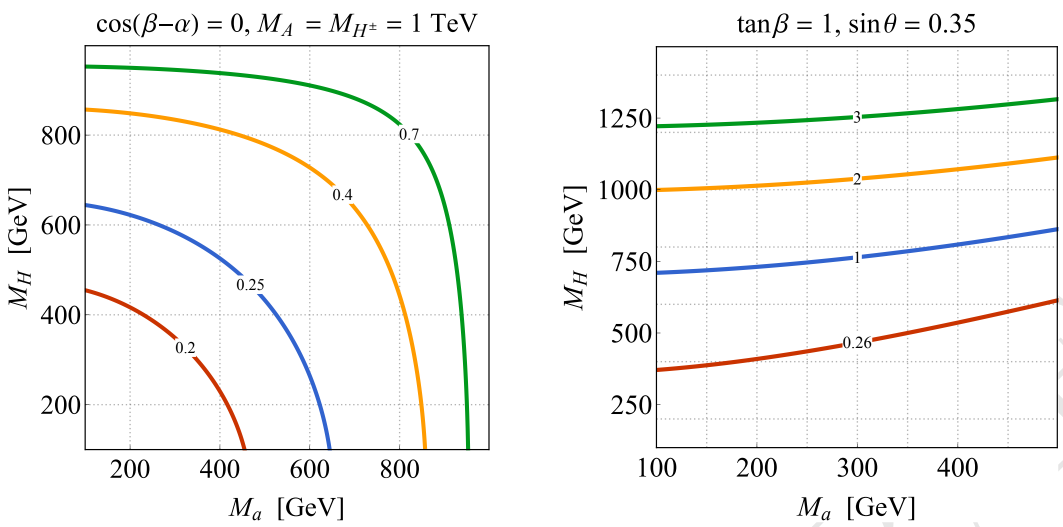

Figure 4: Left: Values of M_a and M_H allowed by EW precision constraints assuming $\cos(\beta - \alpha) = 0$, $M_A = M_{H^\pm} = 1\,\text{TeV}$ and four different values of $\sin\theta$, as indicated by the contour labels. The parameter space below and to the left of the contours is excluded. Right: Constraints in the M_a–M_H plane following from the requirements of having a BFB 2HDM+a scalar potential. The shown results correspond to $\tan\beta = 1$, $\sin\theta = 0.35$ and degenerate heavy Higgs masses $M_H = M_A = M_{H^\pm}$. The region above each contour is excluded for the indicated value of λ_3.

$M_H = M_A = M_{H^\pm}$, the following expressions [?]

$$
\begin{aligned}
g_{Haa} &= \frac{1}{M_H v}\Big[\cot(2\beta)\left(2M_h^2 - 2\lambda_3 v^2\right)\sin^2\theta + \sin(2\beta)\left(\lambda_{P1} - \lambda_{P2}\right) v^2 \cos^2\theta\Big]\,, \\
g_{Aha} &= \frac{1}{M_H v}\Big[M_h^2 + M_H^2 - M_a^2 - 2\lambda_3 v^2 + 2\left(\lambda_{P1}\cos^2\beta + \lambda_{P2}\sin^2\beta\right) v^2\Big]\sin\theta\cos\theta\,.
\end{aligned}
\tag{4.3}
$$

Because $\Gamma(H \to aa) \propto g_{Haa}^2$ and $\Gamma(A \to ha) \propto g_{Aha}^2$, the relations (4.3) imply that in order to keep the total widths Γ_H and Γ_A small, parameter choices of the form $\lambda_3 = \lambda_{P1} = \lambda_{P2}$ are well suited.

Benchmark parameter choices

The above discussion motivates the following choice of parameters

$$
\begin{gathered}
M_H = M_A = M_{H^\pm}\,, \quad m_\chi = 10\,\text{GeV}\,, \\
\cos(\beta - \alpha) = 0\,, \quad \tan\beta = 1\,, \quad \sin\theta = 0.35\,, \\
y_\chi = 1\,, \quad \lambda_3 = \lambda_{P1} = \lambda_{P2} = 3\,.
\end{gathered}
\tag{4.4}
$$

In these type-II 2HDM+a benchmark scenarios the only free parameters are then M_H and M_a. We will study the sensitivity of the existing mono-X searches in the corresponding two-dimensional parameter plane in Section 8. Parameter scans in the M_a–$\tan\beta$ plane

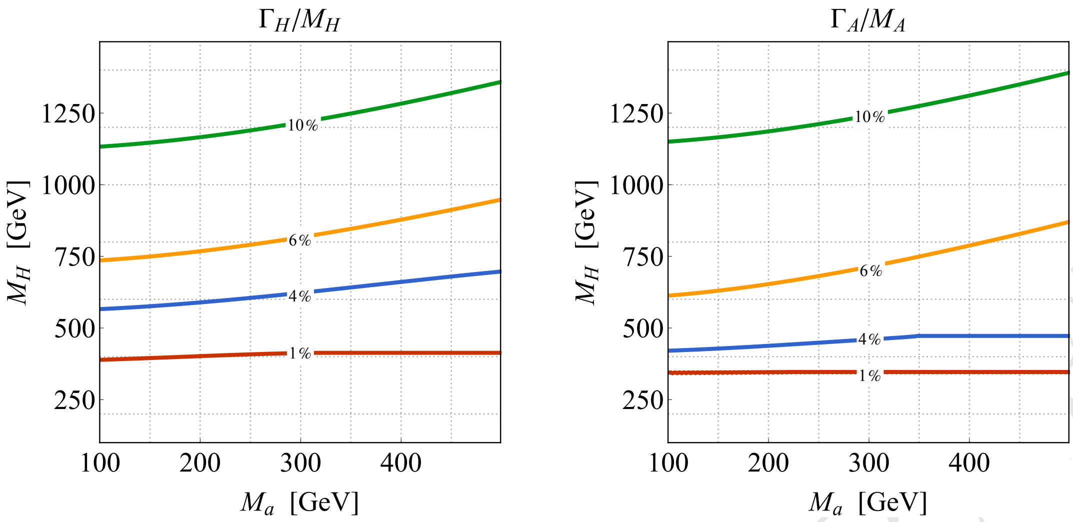

Figure 5: Predictions for Γ_H/M_H (left panel) and Γ_A/M_A (right panel). The shown results correspond to the type-II 2HDM+a benchmark parameter choices given in (4.4).

can also be found in this section. Apart from $\tan\beta$ which will be not fixed to 1 but allowed to vary freely, the latter scans will adopt the choices (4.4) with

$$M_H = M_A = M_{H^\pm} = 600\,\text{GeV}\,. \tag{4.5}$$

At this point is seems worthwhile to add that the mono-X signatures that are most sensitive to the mass splitting between the H and the A, the parameter $\sin\theta$ and the quartic couplings λ_3, λ_{P1}, λ_{P2} turn out to be the mono-Higgs and mono-Z channels (see Section 6 for details). Four benchmark scenarios that illustrate these model dependences have been proposed and studied in [?]. We believe that the specific benchmarks chosen in (4.4) and (4.5) nicely exemplify the rich structure of $E_T^{\rm miss}$ signatures in the 2HDM+a model, and they should therefore serve well as a starting point for further more detailed experimental and theoretical investigations. Further parameter scans will be suggested in Section 11.

As a final validation (or first application) of the proposed benchmark scenario, we present in Figure 5 the predictions for the ratios Γ_H/M_H (left) and Γ_A/M_A (right). We see that the heavy neutral Higgs states H and A are relatively narrow even for values $M_H > 1\,\text{TeV}$ and $M_a = 100\,\text{GeV}$. The narrow width approximation is thus applicable in the entire parameter space considered in our M_a–M_H scans.

5 Comparison to other DM models

In this section we briefly discuss DM models that also feature a 2HDM sector. Our discussion will focus on the similarities and differences between these scenarios and the 2HDM+a model for what concerns the mono-X phenomenology.

2HDM with an extra scalar singlet

Instead of mixing an additional CP-odd singlet P with the pseudoscalar A, as done in (3.5), it is also possible to consider the mixing of a scalar singlet S with the CP-odd spin-0 states h, H. Detailed studies of the direct-detection and relic-density phenomenology of this so-called 2HDM+s model have been presented in [? ?]. Like in the case of the 2HDM+a model, the presence of non-SM Higgs bosons in the 2HDM+s model can lead to novel $E_T^{\rm miss}$ signatures that are not captured by a simplified DM model with just a single scalar mediator. In the pure alignment limit, the most interesting collider signals are mono-Higgs, mono-Z and the $tX+E_T^{\rm miss}$ channels, because these signatures can all arise resonantly. Away from alignment, the scalar mediator couples to the EW gauge bosons and as a result it may also be possible to have a sizeable amount of $E_T^{\rm miss}$ in association with a Z or W boson or in vector boson fusion (VBF). Notice that due to the CP properties of the a the latter $E_T^{\rm miss}$ signatures are not present in the 2HDM+a model.

2HDM with doublet-singlet DM

In both the 2HDM+a and the 2HDM+s model the DM particle is a EW singlet. The DM particle may however also be a mixture of a EW singlet and doublet(s) [? ? ? ?], as in the minimal supersymmtric SM where it has both bino and higgsino components. Generically, this is referred to as singlet-doublet DM. The phenomenology of 2HDM models with singlet-doublet DM has been discussed in [? ?]. In these works only the $b+E_T^{\rm miss}$ and $t\bar{t}+E_T^{\rm miss}$ signatures have been considered and found to provide only weak constraints. The recent study [?] suggests that stronger constraints may arise in the 2HDM with doublet-singlet DM from $Z+E_T^{\rm miss}$ and $tX+E_T^{\rm miss}$ searches. This feature warrants further investigations.

2HDM with higher-dimensional couplings to DM

A gauge-invariant DM model where a pseudoscalar is embedded into a 2DHM that has renormalisable couplings to SM fields but an effective coupling to DM via the dimension-five operator $H_1^\dagger H_2 \bar{\chi}\gamma_5\chi$ has been discussed in [?]. It has been shown that such an effective DM coupling can be obtained in different UV completions such as the 2HDM+a model or a 2HDM with doublet-singlet DM by integrating out heavy particles. Apart from the $tX+E_T^{\rm miss}$ signatures, the whole suit of mono-X signals has been considered in [?]. It was found that a resonant mono-Z signal via $pp \to H \to AZ \to Z+\chi\bar{\chi}$ is a universal prediction in all DM pseudoscalar mediator models, while other signatures such as mono-Higgs are model dependent. Given that a sizeable $H^\pm \to AW$ rate is also a generic feature of DM pseudoscalar models if $M_{H^\pm} > M_A + M_W$, channels like $tW+E_T^{\rm miss}$ [?] should also provide relevant constraints on the DM model introduced in [?].

Inert doublet model

In the scenarios discussed so far the DM particle has always been a fermion. The so-called inert doublet model (IDM) [? ? ?] is an intriguing DM model based on a 2HDM sector that can provide DM in the form of the spin-0 resonances H, A. A Z_2 symmetry renders the DM candidate stable and also implies that the bosonic states that originate from the second (dark) Higgs doublet can only be pair-produced. Since the dark scalars do not couple to the SM fermions, $H, A, H^\pm$ production arises in the IDM dominantly from Drell-Yan processes. The IDM offers a rich spectrum of LHC $E_T^{\rm miss}$ signatures that ranges from mono-jet, mono-Z, mono-W, mono-Higgs to VBF + $E_T^{\rm miss}$ [? ? ? ? ? ? ? ? ? ? ?]. While the prospects to probe the IDM parameter space via the mono-jet channel seem to be limited [?], LHC searches for multiple leptons [? ? ? ? ? ?], multiple jets [? ?] or a combination thereof [?] are expected to allow to test the IDM in limits that are not accessible by direct detection of DM or measurements of the invisible decay width of the SM Higgs. Furthermore, in scenarios in which the mass of DM is almost degenerate with $M_{H^\pm}$, searches for disappearing charged tracks provide a rather unique handle on the IDM high-mass regime [?]. Notice that while the IDM can lead to the same $E_T^{\rm miss}$ signals than the 2HDM+a model, the resulting kinematic distributions will in general not be the same, due to the different production mechanisms and decay topologies in the two models. Selection cuts that are optimised for a 2HDM+a interpretation of a given mono-X search will thus often not be ideal in the IDM context. Dedicated ATLAS and CMS analyses of the mono-X signatures in the IDM do unfortunately not exist at the moment. Such studies would however be highly desirable.

2HDM with an extra scalar mediator and scalar DM

The DM scenario proposed in [?] contains like the 2HDM+s model an extra scalar singlet, which however does not couple to a fermionic DM current $\bar{\chi}\chi$ but to the scalar operator χ^2. The latter work focuses on the parameter space of the model where the mediator s is dominantly produced via either $pp \to H + j \to 2s + j \to j + 4\chi$ or $pp \to H \to sh \to h + 2\chi$. The resulting mono-jet and mono-Higgs cross sections however turn out to be safely below the existing experimental limits. In case the mass hierarchy $M_A > M_H + M_Z$ is realised, the channel $pp \to A \to HZ$ is also interesting, since it either leads to a mono-Z or a $Zh + E_T^{\rm miss}$ signature, depending on whether $H \to 2s \to 4\chi$ or $H \to hs \to h\chi^2$ is the leading decay. We add that an effective version of the model brought forward in [?] has already been constrained by ATLAS [?] using the mono-Higgs channel.

6 $E_T^{\rm miss}$ signatures and their kinematic distributions

The mono-X phenomenology in the 2HDM+a model is determined by the values of the parameters introduced in (3.7). These model parameters can affect the total signal cross sections of the $E_T^{\rm miss}$ signatures, their kinematic distributions, or both. In this section we will discuss the basic features of the most important mono-X channels and identify the experimental observables that can be exploited to search for them. Our discussion will mainly focus on the benchmark (4.4) but we will also present results for other parameter choices to illustrate how a given parameter affects a certain $E_T^{\rm miss}$ signature. All results in this section are obtained at the parton level (i.e. they are fixed-order prediction that do not include the effects of a parton shower) and employ no or only minimal selection requirements.

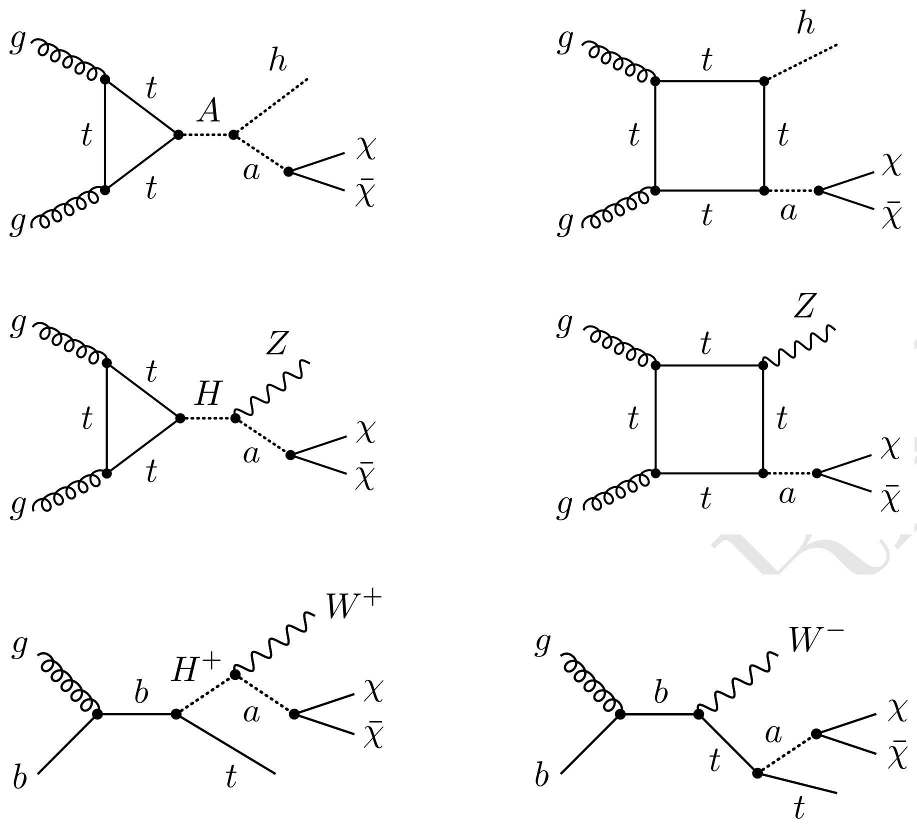

Figure 6: Example diagrams that give rise to a $h + E_T^{\rm miss}$ (upper row), $Z + E_T^{\rm miss}$ (middle row) and $tW + E_T^{\rm miss}$ (lower row) signal in the 2HDM+a model. For further details consult the main text.

6.1 Resonant $E_T^{\rm miss}$ signatures

In the 2HDM+a model there are broadly speaking two different kinds of $E_T^{\rm miss}$ signatures. Signals of the first type can be resonantly produced and channels such as $h+E_T^{\rm miss}$, $Z+E_T^{\rm miss}$ and $tW + E_T^{\rm miss}$ belong to this class. Relevant examples of Feynman graphs are shown in Figure 6. In the case of the mono-Higgs signature, it is evident from the figure that for $M_A > M_h + M_a$ the triangle graph depicted on the left in the upper row allows for resonant mono-Higgs production. Similar resonance enhancements arise from the diagram on the left-hand side for the mono-Z (middle row) and $tW + E_T^{\rm miss}$ (lower row) channel if $M_H > M_Z + M_a$ and $M_H^{\pm} > M_W + M_a$, respectively. Notice that resonant $h + E_T^{\rm miss}$, $Z + E_T^{\rm miss}$ and $tW + E_T^{\rm miss}$ production is not possible in the spin-0 DM models proposed by the DM forum (DMF) [**?**] because in these models the mediators couple only to fermions at tree level. As a result only diagrams of the type shown on the right-hand side of the latter figure are present in these models.

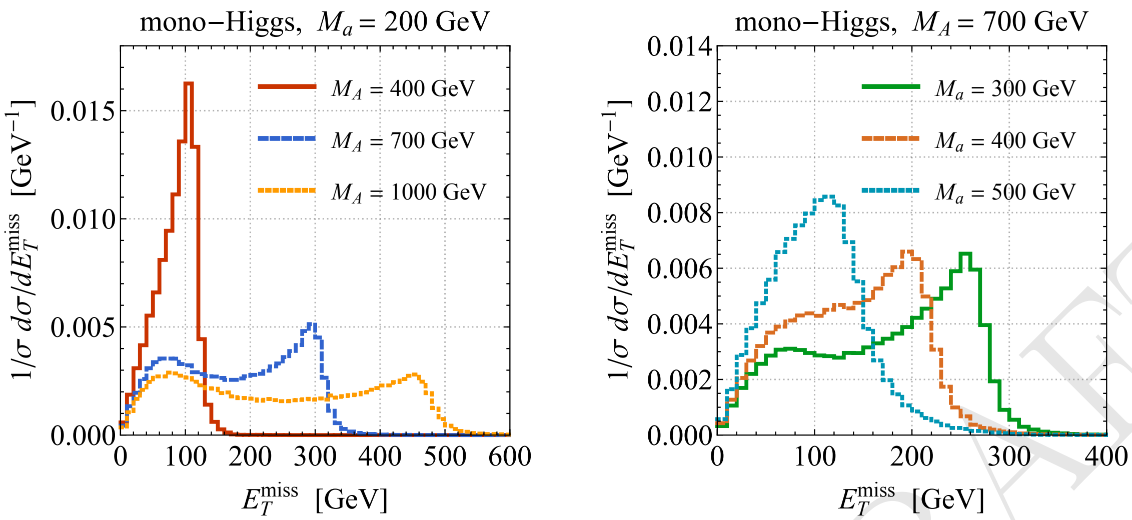

Figure 7: Normalised $E_T^{\rm miss}$ distributions of mono-Higgs production in the 2HDM+a model for different values of M_A and M_a as indicated in the legends. The shown results correspond to the benchmark parameter choices introduced in (4.4).

Mono-Higgs signature

Processes that are resonantly enhanced in the 2HDM+a model have in common that they involve the on-shell decay of a heavy Higgs $H, A, H^\pm$ to a SM particle and the mediator a, which itself subsequently decays to a pair of DM particles. The kinematics of the process $A \to BC$ is governed by the two-body phase space for three massive particles

$$\lambda(m_A, m_B, m_C) = (m_A^2 - m_B^2 - m_C^2)^2 - 4m_B^2 m_C^2\,, \tag{6.1}$$

and this quantity determines the characteristic shape of resonant $E_T^{\rm miss}$ signals in the context of the 2HDM+a model. For instance, in the case of the mono-Higgs signal the $E_T^{\rm miss}$ spectrum will have a Jacobian peak with an endpoint at [**? ?**]

$$E_{T,\rm max}^{\rm miss} \simeq \frac{\lambda^{1/2}(M_A, M_h, M_a)}{2M_A^2}\,, \tag{6.2}$$

for all mass configurations that satisfy $M_A > M_h + M_a$.

In Figure 7 we show the predictions for the normalised $E_T^{\rm miss}$ distribution of $h + E_T^{\rm miss}$ production in the 2HDM+a model for different Higgs masses M_A and M_a. Besides the indicated values of M_A and M_a the parameters used are those given in (4.4). As can be seen from the figure, increasing M_A (M_a) shifts the endpoint of the Jacobian peak to higher (lower) $E_T^{\rm miss}$ values as expected from (6.2). A second feature that is also visible is the plot is that for large mass splittings $M_A - M_a$, the $E_T^{\rm miss}$ spectra develop a pronounced low-$E_T^{\rm miss}$ tail. The events in these tails arise dominantly from the box diagram shown on the right in the upper row of Figure 6. One can also see that these non-resonant contributions interfere with the resonant contributions that stem from triangle graphs. Due to the interplay of resonant and non-resonant contributions the exact shape of the

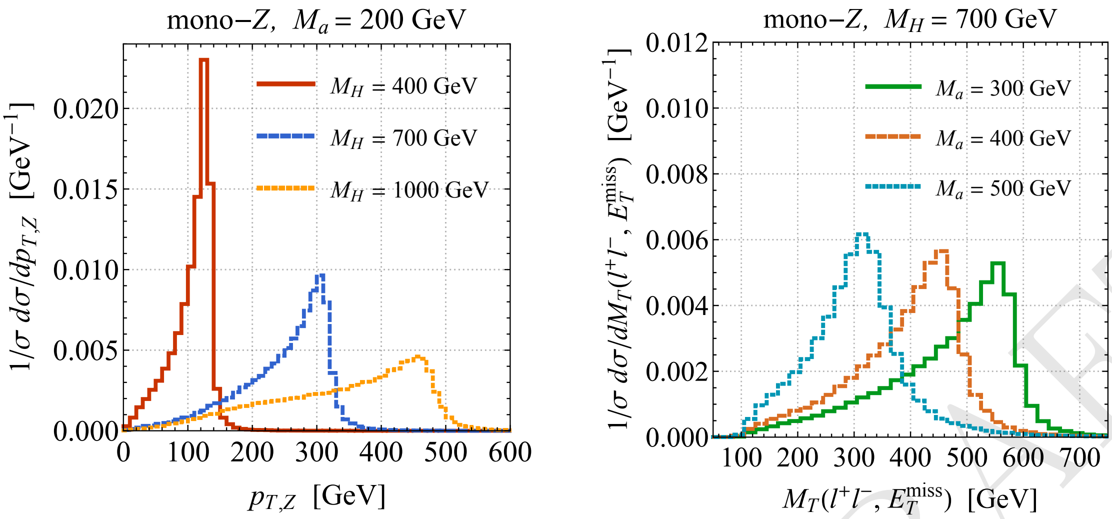

Figure 8: Normalised $p_{T,Z}$ (left panel) and $M_T(\ell^+\ell^-, E_T^{\rm miss})$ (right panel) distributions for $Z+E_T^{\rm miss}$ production followed by $Z \to \ell^+\ell^-$. The shown predictions have been obtained for the 2HDM+a benchmark parameter choices given in (4.4) and employ different values of M_H and M_a as indicated in the legends.

$E_T^{\rm miss}$ distribution is away from the endpoint (6.2) a non-trivial function of the 2HDM+a parameters (3.7).

At the LHC a mono-Higgs signal has so far been searched for in the $h \to \gamma\gamma$ and the $h \to b\bar{b}$ channel (see [? ? ?] for the latest ATLAS and CMS results). While both searches use $E_T^{\rm miss}$ as the main selection variable to discriminate signal from background, the $h\,(\gamma\gamma)+E_T^{\rm miss}$ channel is sensitive to lower $E_T^{\rm miss}$ values than the $h\,(b\bar{b})+E_T^{\rm miss}$ channel, which is otherwise more sensitive to smaller $h+E_T^{\rm miss}$ production cross sections. This feature makes the two modes complementary in the sense that a models with small splittings $M_A - M_a$ are best probed in the former channel, while realisations with a larger mass hierarchy can be well tested via the latter final state. The decay channel $h \to WW$ also offers interesting prospects to search for a mono-Higgs signal in the 2HDM+a model [?] but as yet has not been studied by the LHC collaborations. Auxiliary figures showing mono-Higgs distributions in the 2HDM+a model can be found in Appendix **??**.

Mono-Z signature

Like for the mono-Higgs signal also in the mono-Z case shape analyses of the $E_T^{\rm miss}$ variable offer a powerful way to enhance the signal-to-backround ratio. The endpoint of the $E_T^{\rm miss}$ spectrum for the $Z+E_T^{\rm miss}$ signature can be simply obtained from (6.2) by the replacements $M_A \to M_H$ and $M_h \to M_Z$. Plots that show the corresponding $E_T^{\rm miss}$ distributions can be found in Appendix **??**. Since the four-momenta of the decay products Z and a that enter $H \to Za$ are fixed by H being preferentially on-shell, also the spectrum of the Z-boson transverse momentum ($p_{T,Z}$) in mono-Z production will have a characteristic shape if $M_H > M_Z + M_a$. In fact, the $p_{T,Z}$ distribution is like the $E_T^{\rm miss}$ spectrum predicted to be Jacobian with a cut-off at [? ?]

$$p_{T,Z}^{\max} \simeq \frac{\lambda^{1/2}(M_H, M_Z, M_a)}{2M_H^2}\,, \tag{6.3}$$

that is smeared by the total decay width Γ_H of the heavy Higgs H. Notice that ignoring higher-order corrections, parton-shower and detector effects the shapes of the $p_{T,Z}$ and E_T^{miss} spectra are identical. Whether a shape fit to E_T^{miss} or $p_{T,Z}$ provides a better experimental reach thus depends to first approximation only on which of the two variables can be better measured.

Another useful observable to study the properties of processes involving visible and invisible decay production is the transverse mass

$$M_T(A,B) = \sqrt{m_A^2 + m_B^2 + 2\left(E_{T,A}E_{T,B} - \vec{p}_{T,A} \cdot \vec{p}_{T,B}\right)}\,, \tag{6.4}$$

where $E_{T,A}$ ($E_{T,B}$) denotes the transverse energy of the final-state configuration A (B) and $\vec{p}_{T,A}$ ($\vec{p}_{T,B}$) is the corresponding transverse momentum three-vector. In the case of the mono-Z search that looks for the leptonic decay of the Z boson, the transverse mass can be constructed from the $\ell^+\ell^-$ system and the amount of E_T^{miss}.

Figure 8 displays $p_{T,Z}$ and $M_T(\ell^+\ell^-, E_T^{\text{miss}})$ distributions for different choices of the masses M_H and M_a. The parameters not explicitly specified in the plots have been fixed to the values reported in (4.4). One observes that the differential distributions in $p_{T,Z}$ and $M_T(\ell^+\ell^-, E_T^{\text{miss}})$ have Jacobian peaks, a feature that reflects the resonant production of a H with the subsequent decay $H \to Za \to \ell^+\ell^-\chi\bar{\chi}$. Increasing M_H (M_a) again shifts the endpoints of the distributions to higher (lower) values of $p_{T,Z}$ and $M_T(\ell^+\ell^-, E_T^{\text{miss}})$. Like in the mono-Higgs case, for large mass differences $M_H - M_a$, box diagrams lead to a non-negligible mono-Z rate at low values of $p_{T,Z}$ and $M_T(\ell^+\ell^-, E_T^{\text{miss}})$. Compared to the $h+E_T^{\text{miss}}$ signature the interference effects between resonant and non-resonant contributions are however less pronounced in the $Z + E_T^{\text{miss}}$ case. Plots showing additional mono-Z distributions are provided in Appendix **??**.

The existing LHC searches for a mono-Z signal (cf. [? ?] for the most recent results) have focused either on invisible decays of the SM-like Higgs boson or on topologies where the Z boson is produced in the form of initial-state radiation (ISR). Since ISR of a Z boson is compared to the radiation of a gluon suppressed by both the coupling of the Z and its mass, the mono-Z signal is generically not a discovery channel in models that lead to ISR-like mono-X signatures. In contrast, in the 2HDM+a model the $Z + E_T^{\text{miss}}$ sensitivity turns out to be typically better than the one of the mono-jet channel.

The above discussion has focused on the leptonic decay of the Z boson but searching for a mono-Z signal in the hadronic channel is also possible. In fact, the hadronic and leptonic signatures are complementary, since hadronic decays of the Z boson are more frequent than leptonic decays, but suffer from larger backgrounds. An improved background suppression is possible if "boosted" event topologies are studied, making the hadronic mono-Z signature an interesting channel if the 2HDM+a model includes high-mass Higgs states. Further details on $q\bar{q} + E_T^{\text{miss}}$ search strategies can be found in Appendix **??**.

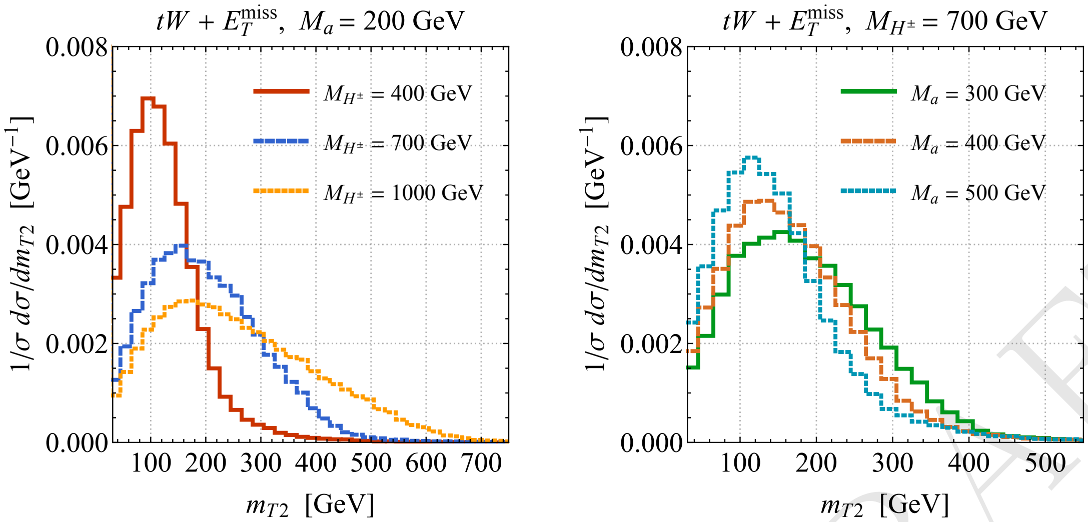

Figure 9: Normalised m_{T2} distributions for $tW + E_T^{\rm miss}$ production in the double-lepton channel. The shown results correspond to the 2HDM+a benchmark (4.4) and employ different values of $M_{H^\pm}$ and M_a as indicated in the legends.

Single-top signatures

Single-top production in association with $E_T^{\rm miss}$ has also been shown to be a promising mono-X channel in the case of spin-0 models [? ? ?]. One can study single-top production in the s-channel, t-channel or in association with a W boson. In the following, we will focus on the $tW + E_T^{\rm miss}$ channel, which in the context of the 2HDM+a model has been identified as the most interesting mode [?]. Example diagrams leading to a $tW + E_T^{\rm miss}$ signature are shown in the lower row of Figure 6. The $tW + E_T^{\rm miss}$ signal can be searched for in the single-lepton and double-lepton final state. Analysis strategies for both channels have been developed in [?]. In the former case $M_T(\ell, E_T^{\rm miss})$ and the asymmetric transverse mass am_{T2} [? ?] can be used to discriminate between signal and background, while in the latter case the stransverse mass m_{T2} [? ?] plays a crucial role in the background suppression.

Examples of normalised m_{T2} distributions obtained in the 2HDM+a model are shown in Figure 9. The coloured histograms correspond to different masses $M_{H^\pm}$ and M_a. The parameters not indicated in the legends have been set to the values given in (4.4). One sees from the plots that the shape of the m_{T2} spectrum is sensitive to the values that are chosen for $M_{H^\pm}$ and M_a. In particular, the maximum of the m_{T2} distribution is shifted to higher values for larger (smaller) values of $M_{H^\pm}$ (M_a). Notice that for heavy charged Higgses the m_{T2} spectrum develops a pronounced high-m_{T2} tail. This feature can be traced back to the resonant contribution $bg \to tH^+ \to tW^+a \to tW^+\chi\bar{\chi}$ (see lower left graph in Figure 6). At present, dedicated ATLAS and CMS analyses of the $tW + E_T^{\rm miss}$ or other single-top-like signatures with $E_T^{\rm miss}$ do not exist. Performing such studies would however be worthwhile since enhanced single-top signatures are expected to appear in many DM model that features an extended Higgs sector.

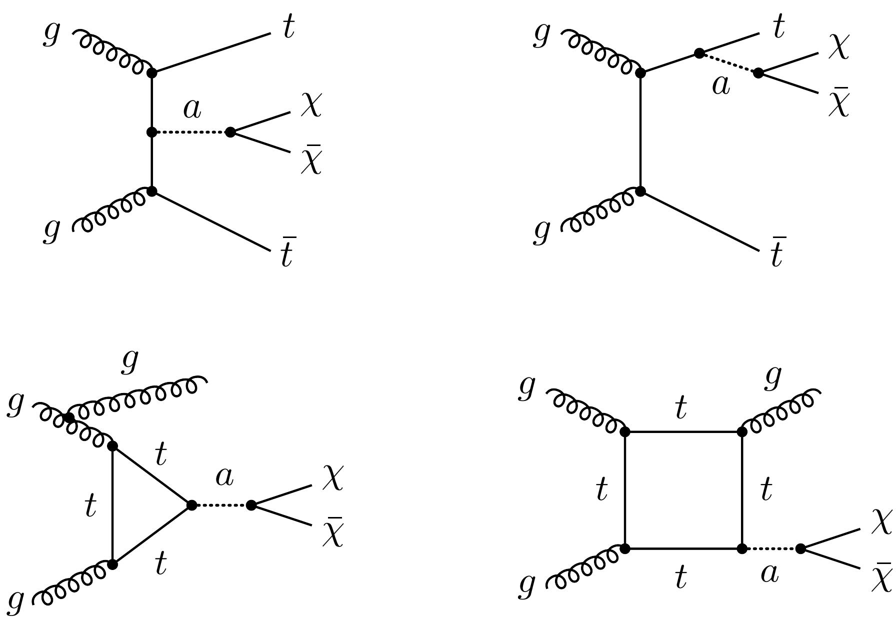

Figure 10: Prototype diagrams that lead to a $t\bar{t}+E_T^{\rm miss}$ (upper row) and $j+E_T^{\rm miss}$ (lower row) signal in the 2HDM+a model. Graphs involving a heavier pseudoscalar A also contribute to the signals but are not shown explicitly.

6.2 Non-resonant $E_T^{\rm miss}$ signatures

Besides the resonant $E_T^{\rm miss}$ signatures discussed in the last subsection the 2HDM+a model also gives rise to non-resonant mono-X signatures. The most important channels in this class are $t\bar{t}+E_T^{\rm miss}$ and $j+E_T^{\rm miss}$ production, but also the $b\bar{b}+E_T^{\rm miss}$ mode is interesting because its rate is $\tan\beta$ enhanced if a Yukawa sector of type-II is realised. Representative Feynman graphs leading to the first two signatures are depicted in Figure 10. Notice that for $M_A \gg M_a > 2m_\chi$ the dominant contribution to the $t\bar{t}+E_T^{\rm miss}$ and mono-jet signals arise from graphs involving the mediator a. In this limit the normalised kinematic distributions of the $t\bar{t}+E_T^{\rm miss}$ and $j+E_T^{\rm miss}$ signals in the 2HDM+a model therefore resemble the shapes of the spectra obtained in the DMF pseudoscalar model. Since the contributions associated to a and A exchange interfere with each other, shape differences can however occur if the pseudoscalars are not widely separated in mass [**?**].

Heavy-quark signatures

Two of the main channels that have been used up to now to search for spin-0 states with large invisible decay widths at the LHC are $t\bar{t}+E_T^{\rm miss}$ and $b\bar{b}+E_T^{\rm miss}$. The latest ATLAS and CMS analyses of this type can be found in [**? ?**]. These searches have been interpreted in the context of the DMF spin-0 models, and for $M_A \gg M_a$ the obtained cross-section

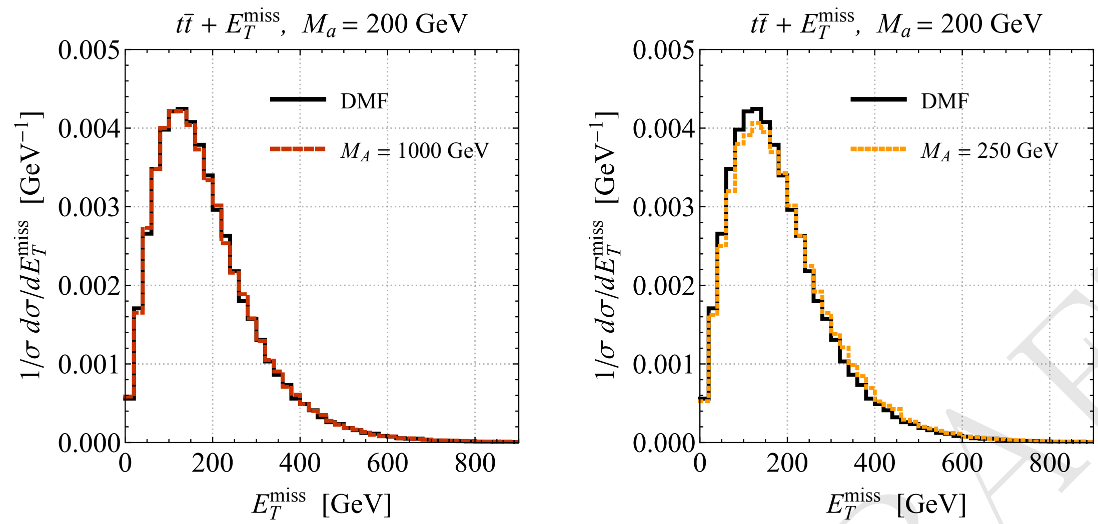

Figure 11: Normalised $E_T^{\rm miss}$ distributions for $t\bar{t} + E_T^{\rm miss}$ production. The black curves correspond to the prediction of the DMF pseudoscalar model, while the coloured predictions illustrate the results in the 2HDM+a benchmark model (4.4) for two different choices of M_A and M_a.

limits can be used to derive exclusion bounds in the 2HDM+a model by using [?]

$$\frac{\sigma\left(pp \to t\bar{t} + E_T^{\rm miss}\right)_{\rm 2HDM+a}}{\sigma\left(pp \to t\bar{t} + E_T^{\rm miss}\right)_{\rm DMF}} \simeq \left(\frac{y_\chi \sin\theta}{g_\chi g_q \tan\beta}\right)^2 . \tag{6.5}$$

Here g_χ (g_q) denotes the DM-mediator (universal quark-mediator) coupling in the DMF pseudoscalar model, and an analog formula holds in the case of the $b\bar{b} + E_T^{\rm miss}$ signature with $\tan\beta$ replaced by $\cot\beta$ in the type-II 2HDM+a model.

In Figure 11 we compare two normalised $E_T^{\rm miss}$ spectra obtained in the 2HDM+a model (coloured histograms) to the prediction of the DMF pseudoscalar model (black histograms). The left panel illustrates the case $M_A \gg M_a$, and one observes that the shape of the 2HDM+a distribution resembles the one of the DMF model within statistical uncertainties. As shown in the plot on the right-hand side, shape distortions instead arise if the particle masses M_A and M_a are not widely separated. Similar findings apply to other variables such as m_{T2} which plays a crucial role in suppressing the $t\bar{t}$ background in two-lepton analyses of the $t\bar{t} + E_T^{\rm miss}$ signature [? ?]. It follows that in order to accurately reproduce the kinematic distributions of the signal in the entire 2HDM+a parameter space, one should not rely on (6.5) but should use a more sophisticated method. A general approach that allows to faithfully translate existing limits on DMF spin-0 models into the 2HDM+a parameter space is described in Appendix A. There it is also shown that this rescaling procedure reproduces the results of a direct Monte Carlo (MC) simulation. In Appendix B we furthermore demonstrate that the same findings apply to the $t\bar{t} + E_T^{\rm miss}$ signature in the 2HDM+s model (see Section 5 for a brief discussion of the model).

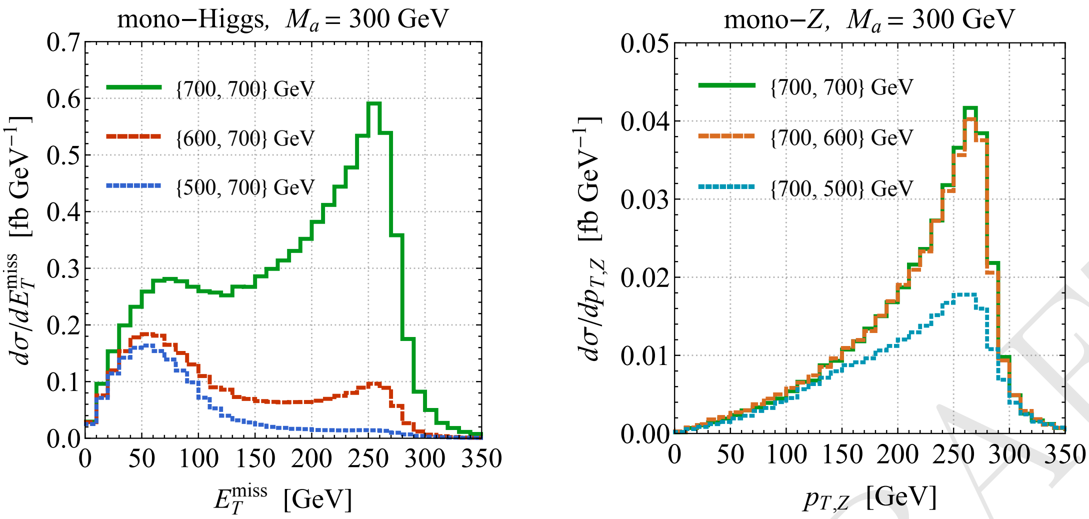

Figure 12: $E_T^{\rm miss}$ ($p_{T,Z}$) distributions for mono-Higgs (mono-Z) production at 13 TeV in the 2HDM+a model. The shown predictions correspond to different sets $\{M_H, M_A\}$ of masses and employ $M_{H^\pm} = \min(M_H, M_A)$, $M_a = 300$ GeV as well as the parameters (4.4).

Mono-jet signature

At the LHC the most studied mono-X signal is the $j + E_T^{\rm miss}$ channel (the newest analyses have been presented in [? ?]) because this mode typically provides the strongest $E_T^{\rm miss}$ constraints on models with ISR-type signatures. Since only loop diagrams where a mediator couples to a quark (see the graphs in lower row in Figure 10) contribute to the mono-jet signature in both the 2HDM+a and the DMF spin-0 models, the normalised kinematic distributions of the $j + E_T^{\rm miss}$ signal turn out to be very similar in these models. In the case that the 2HDM pseudoscalar A is decoupled, i.e. $M_A \gg M_a$, one can use a relation similar to the one shown in (6.5) to translate the existing mono-jet results on the DMF pseudoscalar model into the 2HDM+a parameter space, while in general one can apply the recasting procedure detailed in Appendix A.

6.3 Parameter variations

The kinematic distributions shown in Sections 6.1 and 6.2 all employ the parameters (4.4) and consider only variations of the common heavy Higgs mass $M_H = M_A = M_{H^\pm}$ and the mediator mass M_a. In this subsection we study the impact that modifications of the parameters away from the proposed 2HDM+a benchmark scenarios have. The discussion will thereby focus on the mono-Higgs and mono-Z signatures since the rates and kinematic distributions of these two channels turn out to be most sensitive to parameter changes.

Variations of M_H and M_A

In Figure 12 we display $E_T^{\rm miss}$ distributions in $h + E_T^{\rm miss}$ production (left panel) and $p_{T,Z}$ distributions in $Z + E_T^{\rm miss}$ production (right panel) for different M_H and M_A values. As indicated, the coloured histograms correspond to different choices of $M_{H,A}$ and

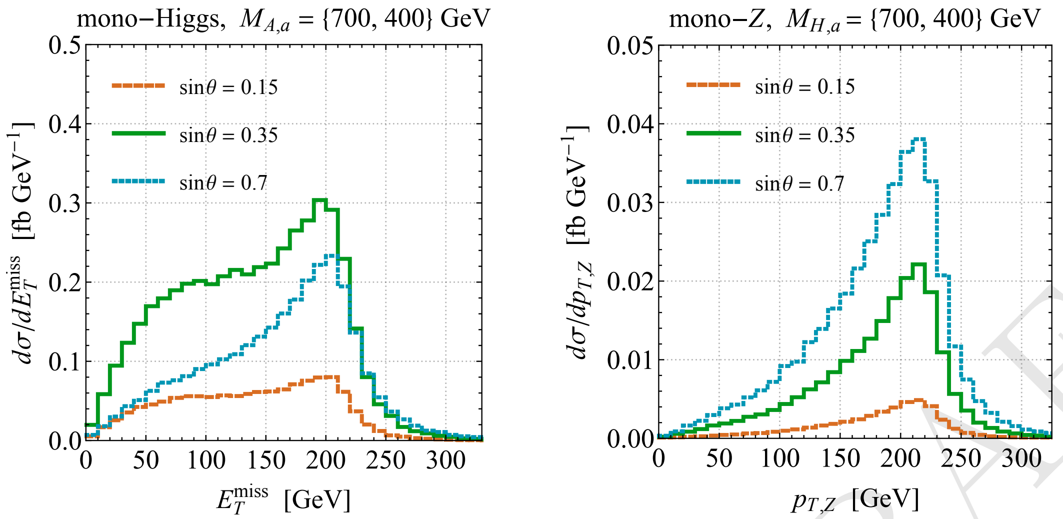

Figure 13: $E_T^{\rm miss}$ ($p_{T,Z}$) distributions for mono-Higgs (mono-Z) production at 13 TeV in the 2HDM+a model. The displayed results correspond to different choices of $\sin\theta$. The remaining parameters are fixed to (4.4) using $M_H = M_A = M_{H^\pm} = 700\,\text{GeV}$ and $M_a = 400\,\text{GeV}$.

$M_{H^\pm} = \min(M_H, M_A)$, but all employ $M_a = 300\,\text{GeV}$. From the figure it is evident that the inclusive mono-Higgs (mono-Z) cross section is reduced compared to the benchmark prediction if M_H (M_A) is taken to be smaller than M_A (M_H). We furthermore observe that a change of M_H strongly affects the shape of the $E_T^{\rm miss}$ distribution, while the distortions in the $p_{T,Z}$ distribution under variations of M_A are much less pronounced. The strong M_H-dependence of the $E_T^{\rm miss}$ spectrum in $h + E_T^{\rm miss}$ production can be traced back to the structure of the coupling g_{Aha}. From (4.3) one sees that for smaller M_H also g_{Aha} is smaller, leading to a reduced $A \to ha$ branching ratio and in turn to a lower rate of resonant production. In contrast, the coupling $g_{HZa} \propto \sin\theta$ that drives resonant production in the case of the mono-Z signal does not depend on the value of M_A.

In order to minimises the constraints from EW precision observables (see the discussion in Section 4) we have chosen $M_H = M_{H^\pm}$ in the the benchmark scenario (4.4). The further choice of having a common 2HDM Higgs mass $M_H = M_A = M_{H^\pm}$ is then motivated by the observation that in such a case both the $h+E_T^{\rm miss}$ and $Z+E_T^{\rm miss}$ signature are dominated by resonant production. While in our sensitivity studies presented in the next section we will always employ the choice $M_H = M_A = M_{H^\pm}$, in future 2HDM+a interpretations of mono-X searches one might however also want to consider cases with $M_H \neq M_A$.

Variation of $\sin\theta$

Figure 13 shows $E_T^{\rm miss}$ distributions in $h+E_T^{\rm miss}$ production (left panel) and $p_{T,Z}$ distributions in $Z+E_T^{\rm miss}$ production (right panel) for different values of $\sin\theta$. The spin-0 masses are chosen as $M_H = M_A = M_{H^\pm} = 700\,\text{GeV}$ and $M_a = 400\,\text{GeV}$, and the remaining parameters are fixed to (4.4). From the two panels it is evident that a variation of $\sin\theta$ leads to both a rate and shape change in the case of the mono-Higgs signal, while in the

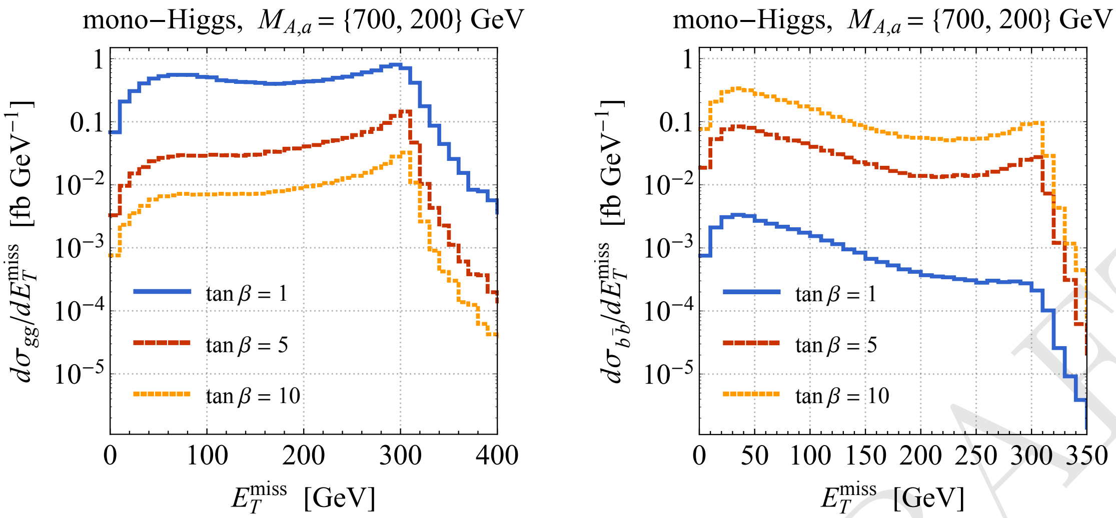

Figure 14: $E_T^{\rm miss}$ distributions for mono-Higgs production in gg-fusion (left panel) and $b\bar{b}$-fusion (right panel) in the 2HDM+a model. The displayed results correspond to pp collisions at 13 TeV and different choices of $\tan\beta$. The parameters not detailed in the plots are set to (4.4) using $M_H = M_A = M_{H^\pm} = 700\,\text{GeV}$ and $M_a = 200\,\text{GeV}$.

case of the mono-Z channel only the total cross section gets rescaled to first approximation. The strong sensitivity of the shape of the $E_T^{\rm miss}$ spectrum in $h + E_T^{\rm miss}$ production is a again a result of the interplay of resonant and non-resonant contributions. While the $gg \to A \to ha \to h\chi\bar{\chi}$ amplitude scales as $\sin\theta\cos^3\theta$, the $gg \to ha \to h\chi\bar{\chi}$ matrix element shows a $\sin\theta\cos\theta$ dependence. These scalings imply that at small (large) $\sin\theta$ the resonant (non-resonant) amplitudes provide the dominant contribution to the $E_T^{\rm miss}$ distribution in mono-Higgs production. In the case of the mono-Z signal the resonant and non-resonant amplitudes both scale as $\sin\theta\cos\theta$ and in consequence the cross section and all kinematic distributions are essentially not distorted under changes of the mixing angle θ. Notice that the latter statement also holds in the case of the $t\bar{t} + E_T^{\rm miss}$, $b\bar{b} + E_T^{\rm miss}$ and mono-jet signatures. This can be deduced from (6.5).

From the above discussion it follows that the choice $\sin\theta = 0.35$ made in (4.4) leads to an enhanced sensitivity of the mono-Higgs signal to the 2HDM+a parameter space. To perform parameter scans in scenarios with larger mixing angles like $\sin\theta = 0.7$ would however also be worthwhile because such a choice would lead to an improved coverage via the mono-Z channel. We finally note that in scenarios with $\sin\theta > 0.35$ the maximal allowed size of mass splitting $M_H - M_a$ is more constrained by vacuum stability arguments than in (4.4). This is can be seen from (4.2).

Variation of $\tan\beta$

In Figure 14 we display $E_T^{\rm miss}$ distributions in mono-Higgs production for different choices of $\tan\beta$. The left (right) panel illustrates the contributions from the $gg \to h + E_T^{\rm miss}$ ($b\bar{b} \to h + E_T^{\rm miss}$) channel. The shown results have been obtained at 13 TeV and employ (4.4) with $M_H = M_A = M_{H^\pm} = 700\,\text{GeV}$ and $M_a = 200\,\text{GeV}$. One first notices that the total

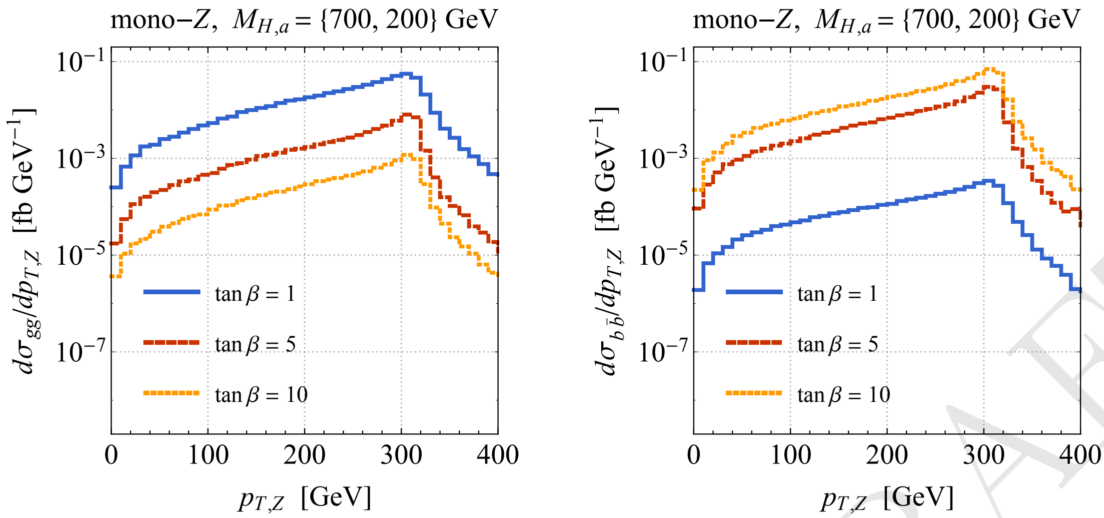

Figure 15: $p_{T,Z}$ distributions for mono-Z production in gg-fusion (left panel) and $b\bar{b}$-fusion (right panel) in the 2HDM+a model. The shown predictions correspond to pp collisions at 13 TeV and the same choices of parameters as in Figure 14 are employed.

production cross section in gg-fusion strongly decreases with increasing $\tan\beta$, while in the case of $b\bar{b}$-fusion the opposite behaviour is observed. The strong depletion/enhancement of the production rates originates from the fact that in the type-II 2HDM+a model considered in this whitepaper the couplings of H, A, a to top quarks are proportional to $\cot\beta$, while the corresponding couplings to bottom quarks are proportional to $\tan\beta$. Numerically, we find that at the inclusive level the gg-fusion and $b\bar{b}$-fusion contributions to mono-Higgs production are comparable in size for $\tan\beta \simeq 5$. This means that for $\tan\beta \gtrsim 5$ both channels have to be included to obtain accurate predictions. From the two panels it is furthermore apparent that variations of $\tan\beta$ do not only change the overall signal strength, but also have a pronounced impact on the shapes of the $E_T^{\rm miss}$ distributions. In particular, changes in $\tan\beta$ influence the importance of resonant versus non-resonant contributions.

Similar to the mono-Higgs channel also for the mono-Z signal $b\bar{b}$-initiated production can be relevant for sufficiently large values of $\tan\beta$ [?]. Figure 15 displays $p_{T,Z}$ spectra in mono-Z production for different choices of $\tan\beta$ in both the gg-fusion (left panel) and $b\bar{b}$-fusion (right panel) channel. From the plots one sees that for the considered parameters $M_H = M_A = M_{H^\pm} = 700\,{\rm GeV}$ and $M_a = 200\,{\rm GeV}$, production in $b\bar{b}$-fusion dominates over gg-fusion already for the choice $\tan\beta = 5$. One also observes that in the mono-Z case the shapes of the differential distributions are less distorted under changes of $\tan\beta$ than the mono-Higgs spectra. For the sake of completeness, we furthermore add that the modifications in the kinematic distributions of $t\bar{t} + E_T^{\rm miss}$ and $j + E_T^{\rm miss}$ production under changes of $\tan\beta$ are like in the mono-Z case not very pronounced.

Our scans in the $M_a - M_H$ plane are based on the choice $\tan\beta = 1$, since for this value the existing mono-Higgs and mono-Z searches already allow to probe/exclude large regions in the mass planes. These scans are complemented by sensitivity studies in the $M_a - \tan\beta$

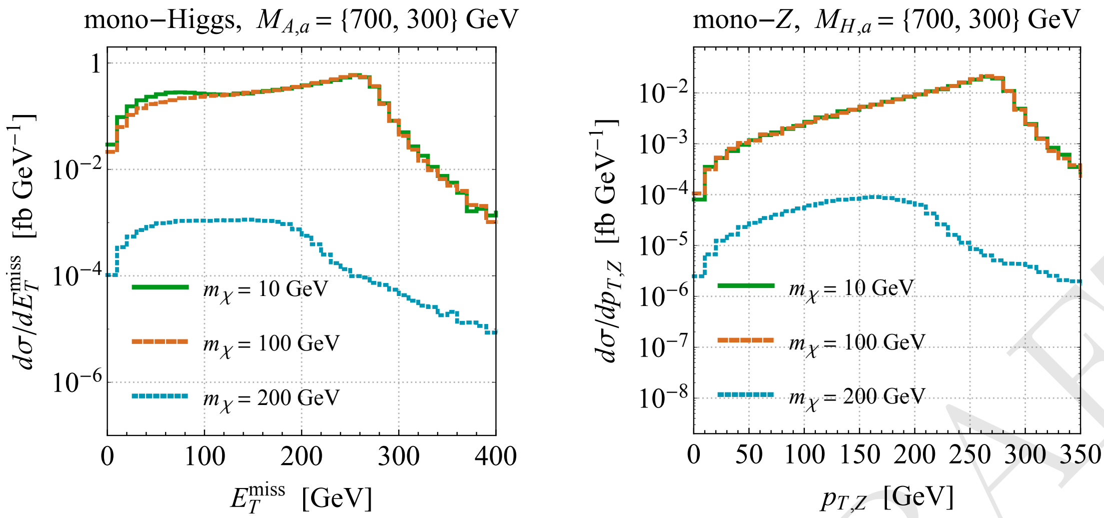

Figure 16: $E_T^{\rm miss}$ ($p_{T,Z}$) distributions for mono-Higgs (mono-Z) production at 13 TeV. The presented results correspond to different values of the DM mass m_χ. The other 2HDM+a parameters are set to (4.4) using $M_H = M_A = M_{H^\pm} = 700\,{\rm GeV}$ and $M_a = 300\,{\rm GeV}$.

(cf. Section 8 and [? ? ?]). We add that if $\tan\beta$ is scanned special attention has to be given to the fact that in the large-$\tan\beta$ limit the total decay widths of some of the Higgs states can become very large, potentially invalidating the narrow width approximation.

Variation of m_χ

The modifications of the $E_T^{\rm miss}$ ($p_{T,Z}$) spectrum in $h+E_T^{\rm miss}$ ($Z+E_T^{\rm miss}$) production under a variation of the DM mass m_χ are illustrated in the two panels of Figure 16. The given predictions correspond to pp collision at 13 TeV and employ the benchmark parameters (4.4) with $M_H = M_A = M_{H^\pm} = 700\,{\rm GeV}$ and $M_a = 300\,{\rm GeV}$. One observes that the depicted scenarios with $M_a > 2m_\chi$ (green and purple histograms) lead to almost identical rates, $E_T^{\rm miss}$ and $p_{T,Z}$ spectra, while the choice $M_a < 2m_\chi$ (blue histograms) largely reduces the total rates and also modifies the shapes of the shown distributions. This feature is expected since for $M_a > m_\chi/2$ the decay channel $a \to \chi\bar{\chi}$ is kinematically allowed, while for $M_a < m_\chi/2$ it is forbidden. In order to have detectable mono-X signals even for light mediators a, we have chosen a value of $m_\chi = 10\,{\rm GeV}$ as the baseline for the following sensitivity studies. We will discuss the role that the DM mass m_χ plays in the context of (in)direct detection and the DM relic density in Section 9 and Section 10, respectively.

7 Non-$E_T^{\rm miss}$ collider signatures

In this section we will discuss the most important non-$E_T^{\rm miss}$ signals that can be used to explore the parameter space of the 2HDM+a model at the LHC. Most of the discussion will be centred around final states containing top quarks since these channels provide the best sensitivity to model realisations with low $\tan\beta$ such as our benchmark parameter

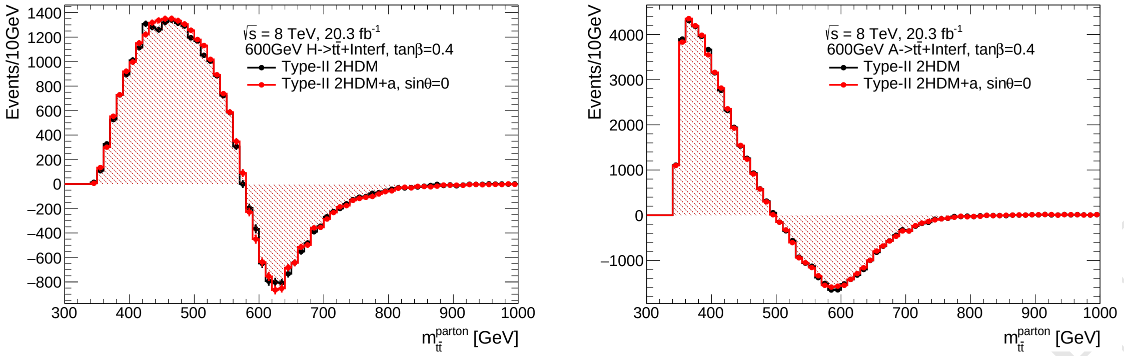

Figure 17: $m_{t\bar{t}}$ spectra for $gg \to H \to t\bar{t}$ (left) and $gg \to A \to t\bar{t}$ (right). The black (red) predictions correspond to the type-II 2HDM (2HDM+a) model. The shown results employ $M_H = M_A = M_{H^\pm} = 600\,\text{GeV}$, $M_a = 100\,\text{GeV}$, $\tan\beta = 0.4$ and $\sin\theta = 0$, and correspond to $20.3\,\text{fb}^{-1}$ of 8 TeV data. The parameters not explicitly specified are chosen as in (4.4). [Uli: Fix notation?]

choice (4.4). Final states that give excess to the 2HDM+a parameter space with large $\tan\beta$ such as di-tau searches will however also be discussed briefly.

7.1 Di-top searches

In all 2HDM models, the spin-0 bosons H, A decay dominantly to top-quark pairs if these states have masses above the top-quark threshold, i.e. $M_{H,A} > 2m_t$, and if $\tan\beta = \mathcal{O}(1)$. New-physics scenarios of this kind can thus be tested by studying the $t\bar{t}$ invariant mass spectrum $m_{t\bar{t}}$. Interference effects between the signal process and the SM $t\bar{t}$ background however distort the $m_{t\bar{t}}$ signal shape from a single peak to a peak-dip structure [**? ? ? ? ?**], a feature that represents a serious obstacle to probe 2HDM models with $M_{H,A} > 350\,\text{GeV}$ and small $\tan\beta$ values [**? ? ? ?**].

The first LHC analysis that takes into account interference effects between the signal process $gg \to H/A \to t\bar{t}$ and the SM background $gg \to t\bar{t}$ is the ATLAS search [**?**]. This search is based on an integrated luminosity of $20.3\,\text{fb}^{-1}$ collected at 8 TeV. The results are interpreted in alignment limit of the usual type-II 2HDM. The obtained exclusion limits in the $M_{H,A}-\tan\beta$ plane turn out to be significantly stronger than previously published LHC constraints on the 2HDM parameter space with low $\tan\beta$ and $M_{H,A} \in [500, 650]\,\text{GeV}$. For instance, for $M_{H,A} = 500\,\text{GeV}$ values of $\tan\beta < 1$ are disfavoured at 95% CL. A similar parameter space can be probed if the results [**?**] are reinterpreted in the context of the 2HDM+a model [**?**].

An assortment of di-top invariant mass spectra corresponding to the 2HDM+a model are shown in Figures 17 and 18. The signal process has been obtained by treating the loop contributions from top and bottom quarks as form factors a la [**?**]. In this way the interference between the signal and the tree-level SM background from $gg \to t\bar{t}$ can be calculated at leading order in QCD. In Figure 17, we show predictions for the $m_{t\bar{t}}$ spectra in $gg \to H \to t\bar{t}$ (left panel) and $gg \to H \to t\bar{t}$ (right panel). The black histograms

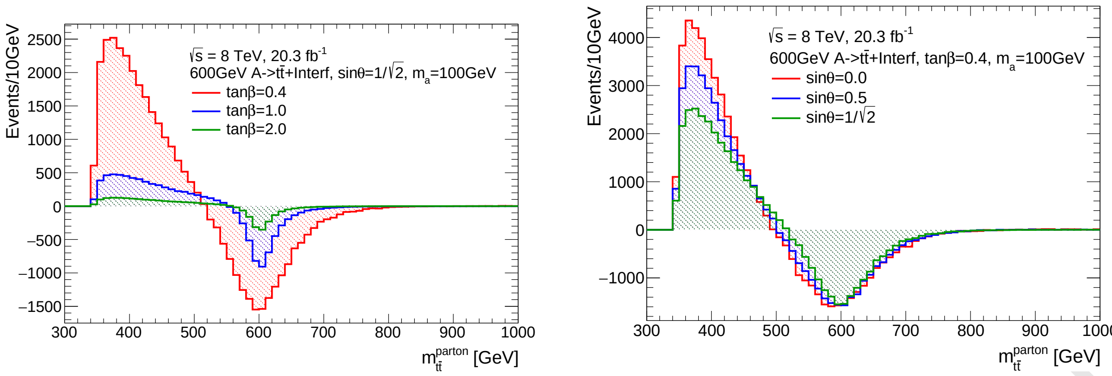

Figure 18: Left: $\tan\beta$ dependency of $m_{t\bar{t}}$ spectrum for fixed $\sin\theta = 1/\sqrt{2}$. Right: $\sin\theta$ dependency of $m_{t\bar{t}}$ spectrum for fixed $\tan\beta = 0.4$. The chosen 2HDM+a parameters are $M_H = M_A = M_{H^\pm} = 600\,\text{GeV}$ and $M_a = 100\,\text{GeV}$ and the depicted distributions correspond to $20.3\,\text{fb}^{-1}$ of integrated luminosity collected at 8 TeV. Parameters not explicitly specified are set to (4.4). [Uli: Fix notation?]

illustrates the 2HDM predictions [?], while the red curves represent the corresponding 2HDM+a predictions for the choice $\sin\theta = 0$, which effectively decouples the mediator a from the 2HDM Higgs sector. The agreement between the black and red predictions serves as a validation of our form factor implementation in the 2HDM+a model.

As examples of the parameter dependences of the $t\bar{t}$ predictions in the 2HDM+a model, we display in Figure 18 several $m_{t\bar{t}}$ spectra in $pp \to A \to t\bar{t}$ either fixing $\sin\theta$ and varying $\tan\beta$ (left panel) or vice versa (right panel). The Higgs masses are chosen $M_H = M_A = M_{H^\pm} = 600\,\text{GeV}$ and $M_a = 100\,\text{GeV}$, which implies that only the decays $H/A \to t\bar{t}$ are kinematically possible but not $a \to t\bar{t}$. From the left panel one sees that increasing $\tan\beta$ leads to a reduction of the signal strength. Likewise, larger values of $\sin\theta$ also lead to lower $t\bar{t}$ cross sections as illustrated on the right-hand side of the latter figure. These are expected features because the $gg \to A$ amplitude scales as $\cot\beta\cos\theta$. One also observes that the interference between the $t\bar{t}$ signal and the corresponding background, and thus the shape of the $m_{t\bar{t}}$ spectrum, depends on the precise choice of $\tan\beta$ and $\sin\theta$. Before moving on, let us add that the results of [?] have already been recasted to the 2HDM+a model in [?]. For the parameter benchmarks studied in the latter paper it turns out that $\tan\beta < \mathcal{O}(0.5)$ values can be probed/excluded based on the 8 TeV ATLAS search, rendering the resulting $t\bar{t}$ constraints weaker than those arising at present from flavour physics (see Section 4).

7.2 Four-top searches

The four-top final state is a rare, yet increasingly important signature, since it will gain sensitivity and thus attention with the LHC collecting more and more luminosity (see for instance [? ? ? ? ? ?]). In fact, in the work [?] the results of a search for the four-top final state based on $13.2\,\text{fb}^{-1}$ of 13 TeV LHC data has already been interpreted in

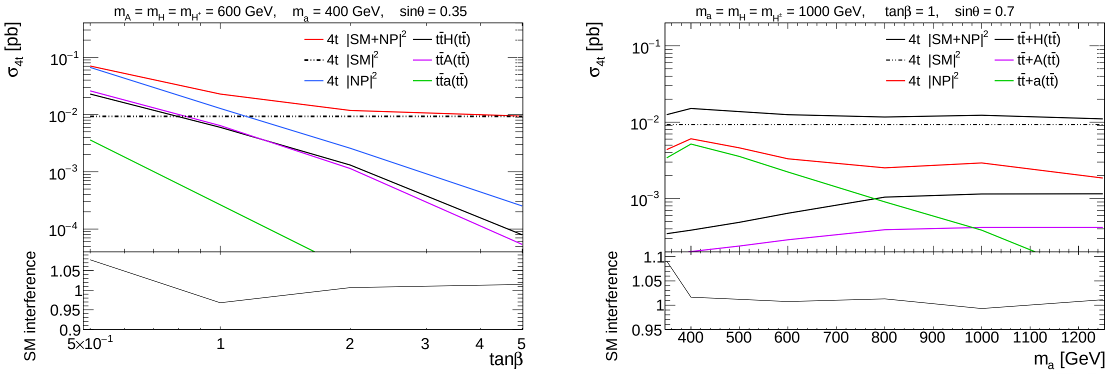

Figure 19: Four-top cross sections as function of $\tan\beta$ (left) and M_a (right) for pp collisions at 13 TeV. In the left panel $M_H = M_A = M_{H^\pm} = 600\,\text{GeV}$ and $M_a = 400\,\text{GeV}$ have been used, while in the right panel $M_H = M_A = M_{H^\pm} = 1\,\text{TeV}$ and $\sin\theta = 0.7$ have been employed. Parameters not explicitly specified are set to (4.4). The SM and the different new-physics contributions are indicated by the black and coloured lines. See text for further explanations. [Uli: Fix notation?]

the context of the normal 2HDM. The comparison to the predictions for a type-II 2HDM in the alignment limit allows the exclusion at the 95% CL of $\tan\beta$ below 0.17 (0.11) for $M_H = 400\,\text{GeV}$ ($M_H = 1\,\text{TeV}$). While these limits are weaker than those that can be obtained from $t\bar{t}$ production in the $M_H \in [500, 650]\,\text{GeV}$ range [**?**], in the long run, four-top searches can be expected to have a better sensitivity than $t\bar{t}$ searches for mediators with masses close to the top threshold and very heavy Higgses.

In this whitepaper we perform a first characterisation of the four-top signature in the 2HDM+a context by studied the predicted cross section for different parameter choices. Predictions for the four-top cross section (σ_{4t}) as a function of $\tan\beta$ (left panel) and M_a (right panel) are presented in Figure 19. The total four-top production cross section in the SM ($|\text{SM}|^2$) is indicated by a black dashed-dotted line in both panels, while the new-physics (NP) contributions ($|\text{NP}|^2$) are represented by the blue curves. The predictions that account for both the SM and the 2HDM+a contribution as well as their interference ($|\text{SM}+\text{NP}|^2$) are coloured red. The contributions from associated $t\bar{t}$ production of an on-shell H, A, a with the subsequent decay $H/A/a \to t\bar{t}$ are also given. A brief description of how the different channels have been separated in our MC simulations is given in Appendix C. From the left panel one can see that for the chosen parameters on-shell production of H and A provides the dominant contribution to inclusive cross section. Interference effects turn out to be small as they modify the results by only $\mathcal{O}(5\%)$ at the inclusive level. This feature is illustrated in the lower part of the left plot.

On the right-hand side in Figure 19 we instead study the M_a dependence of the cross section. One first observes that for the chosen parameters the $|\text{NP}|^2$ contribution is rather flat in M_a. The breakdown of the on-shell contributions furthermore shows that for $M_a \lesssim 800\,\text{GeV}$ the contribution from $t\bar{t}a$ production dominates, while for $M_a \gtrsim 800\,\text{GeV}$ the $t\bar{t}H/A$ channels are numerically more important. The little bump at 1 TeV is due to

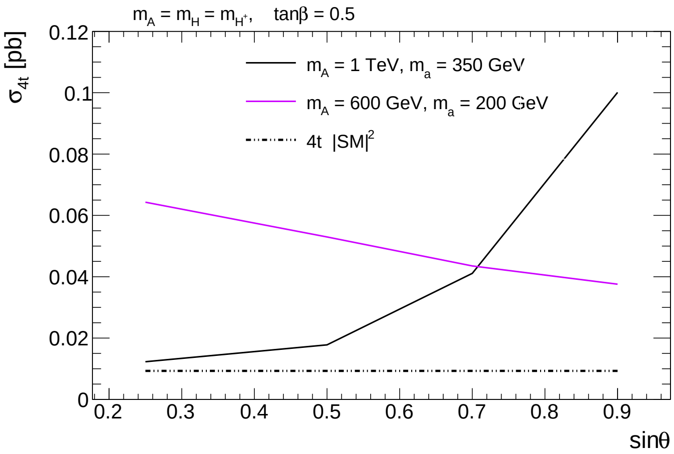

Figure 20: Four-top cross sections as a function of $\sin\theta$ at the 13 TeV LHC. The black dashed-dotted corresponds to the SM prediction, while the solid black (magenta) line employs $M_H = M_A = M_{H^\pm} = 1\,\text{TeV}$ and $M_a = 350\,\text{GeV}$ ($M_H = M_A = M_{H^\pm} = 600\,\text{GeV}$ and $M_a = 200\,\text{GeV}$). Both $|\text{NP}|^2$ curves are based on $\tan\beta = 0.5$ and all parameters not explicitly specified in the legend are set to (4.4). [Uli: Fix notation?]

interference effects between the three Higgs states. As for the previous benchmark, the impact of the signal-background interference on the inclusive cross section is found to be small (i.e. below 2%), except for M_a values close to the top threshold.

In Figure 20 we finally plot the $\sin\theta$ dependence of the new-physics contribution $|\text{NP}|^2$ to the cross section of four-top production for the two benchmarks studied before. One sees that in the case of $M_H = M_A = M_{H^\pm} = 1\,\text{TeV}$ and $M_a = 350\,\text{GeV}$ (black curve) the cross section increases for increasing $\sin\theta$. This is expected because the dominant contribution to the signal arises from $t\bar{t}a$ production followed by $a \to t\bar{t}$ and the coupling of the a to top quarks scales as $\sin\theta$. In the case of $M_H = M_A = M_{H^\pm} = 600\,\text{GeV}$ and $M_a = 200\,\text{GeV}$ (magenta curve) the cross section instead decreases with increasing $\sin\theta$. In this case the $H \to t\bar{t}$ decay gives the largest contribution, since $a \to t\bar{t}$ is kinematically closed. The observed $\sin\theta$ dependence then arises from the interplay between $\Gamma(H \to t\bar{t})$ which does not depend on $\sin\theta$ and $\Gamma(H \to aa)$ as well as $\Gamma(H \to Za)$ which are both proportional to $\sin^2\theta$.

7.3 Other final states

The $\tau^+\tau^-$ final state is one of the most common channels that experiments have considered to search for additional neutral Higgs bosons (see [**?** **?**] for the latest LHC results). The sensitivity of the $\tau^+\tau^-$ to the 2HDM+a parameter space has been studied in the article [**?**]. There it was found that $\tau^+\tau^-$ searches have the strongest sensitivity in the $H \to \tau^+\tau^-$ channel for Higgs masses $M_H \lesssim 2m_t$, $M_a < M_H/2$ and $\tan\beta < \mathcal{O}(1)$. The rates in $A/a \to \tau^+\tau^-$ are, on the other hand, predicted to be generically small if the $A/a \to \chi\bar{\chi}$ decays are open. These findings imply that it will be very difficult to test the benchmark models (4.5) through $\tau^+\tau^-$ searches. Future $\tau^+\tau^-$ analyses may however be able to exclude scenarios a la (4.4) for $M_H = M_A = M_{H^\pm} = \mathcal{O}(300\,\text{GeV})$ and $M_H \lesssim 2M_a$. Since such realisations are not easy to test otherwise, interpreting the results of forthcoming $\tau^+\tau^-$ searches in the 2HDM+a context seems to be worthwhile.

If $M_H > M_a + M_Z$ and the mediator a is sufficiently heavy, i.e. $M_a > 2m_t$, another channel that offers sensitivity to the 2HDM+a parameter space is $pp \to aZ$ with $a \to t\bar{t}$ instead of $a \to \chi\bar{\chi}$ [?]. The corresponding $t\bar{t}Z$ final state has been recently studied [?] in the context of the normal 2HDM and shown to lead to a robust coverage of the 2HDM parameter space with $M_{H,A} > 350\,\text{GeV}$, $|M_H - M_A| > M_Z$ and $\tan\beta = \mathcal{O}(1)$ at future LHC runs. The analysis strategy detailed in [?] can be directly applied to the 2HDM+a case, and should allow to probe model realisations that feature a mediators with masses above the top threshold in the high-luminosity phase of the LHC. Notice that such scenarios are generically difficult to explore via a mono-Z search (see Section 8.2).

The ATLAS and CMS collaborations have set limits on the production of charged Higgses in both the $\tau\nu$ [? ?] and the tb [? ? ?] final state. The limits given in [?] have been used in [?] to derive constraints on the 2HDM+a model. It turns out that the constraints on the 2HDM+a parameter space are generically weaker than those obtained in the 2HDM context, because in the 2HDM+a model the $H^\pm \to tb$ branching tends to be reduced compared to the 2HDM since the partial decay width $H^\pm \to aW^\pm$ is generically non-vanishing. However, compared to the $tW + E_T^{\text{miss}}$ signature, tb searches can still provide complementary information, because the non-E_T^{miss} search can test $M_{H^\pm}$ values below around 350 GeV which are not easily accessible with the corresponding E_T^{miss} signature [?]. Another signal that can be used to search for charged Higgses is the tbW final state [?]. This channel has however not yet been explored in the 2HDM+a context.

8 Sensitivity studies

In this section we present sensitivity estimates for two of the main E_T^{miss} signatures in the 2HDM+a model, namely the $h + E_T^{\text{miss}}$ and the $Z + E_T^{\text{miss}}$ channels. Specifically, we will consider the mono-Higgs (mono-Z) signal in the $b\bar{b}$ ($\ell^+\ell^-$) channel. Our studies are based on parton-level reinterpretation of existing results that use $36\,\text{fb}^{-1}$ of LHC data taken at $\sqrt{s} = 13\,\text{TeV}$. These results contain different amounts of public information. In the mono-Higgs case model-independent limits presented in [?] are used for the reinterpretation, while in the mono-Z case the sensitivity is estimated using parton-level information on the signal together with published background estimates [?]. The sensitivities that other mono-X searches provide are also briefly discussed below. A concise description of how the mono-X signals considered in our sensitivity study have been generated can be found in Appendix C.

8.1 Mono-Higgs study

The sensitivity estimates of the ATLAS and CMS mono-Higgs searches in the $b\bar{b}$ channel to the 2HDM+a model are based on the model-independent limits on the anomalous production of the SM Higgs boson in association with E_T^{miss} derived in [?]. As these limits are set

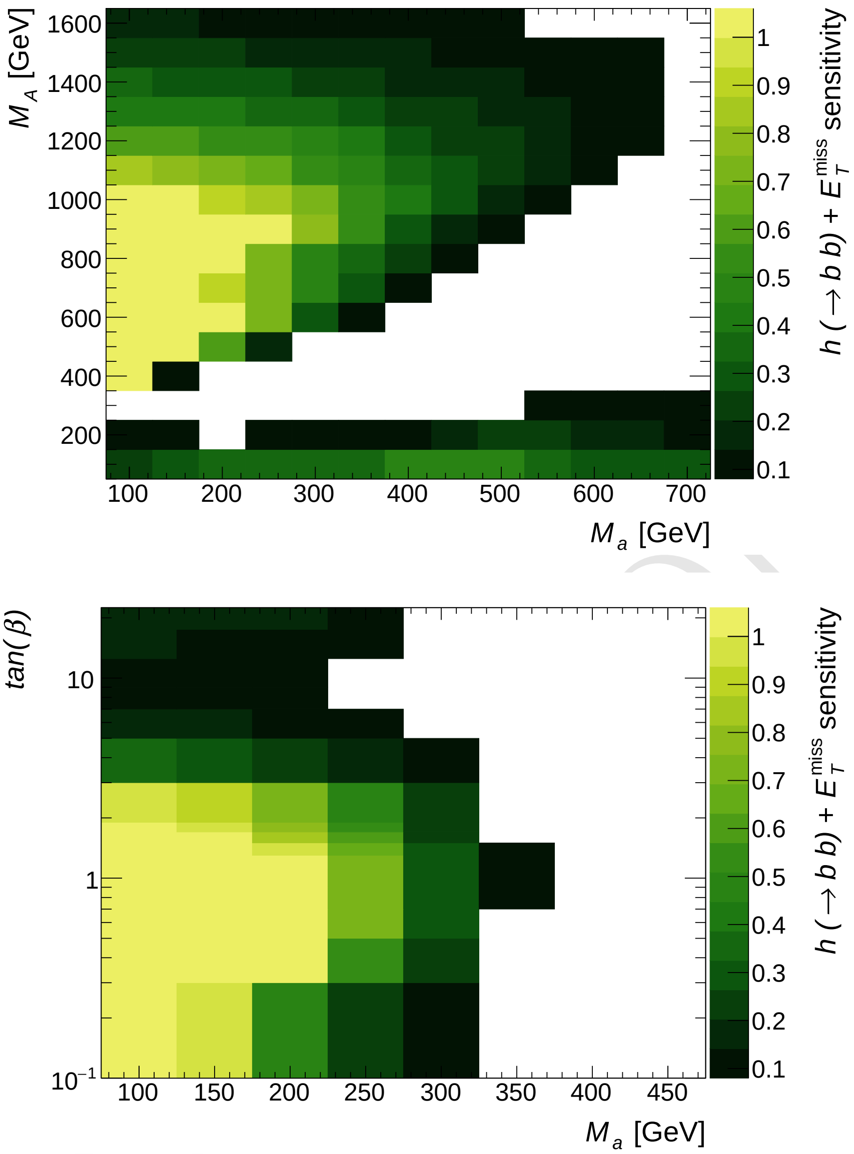

Figure 21: Estimated sensitivities with the $h + E_T^{\rm miss}$ signature in the $h \to b\bar{b}$ channel. The upper (lower) panel shows our results in the M_a–M_A (M_a–$\tan\beta$) plane. The remaining parameters are set to (4.4) in the upper panel, while in the lower panel $\tan\beta$ is left to vary but the common 2HDM Higgs mass is fixed to (4.5). Bins with no content have a negligible sensitivity $S < 0.1$. See text for further explanations. [Uli: Use the same notation etc. for the plots in Figures 21 and 22!]

in terms of the observed production cross section of non-SM events with large $E_T^{\rm miss}$ and a Higgs boson, they can be compared directly to the cross sections obtained in the 2HDM+a model after taking into account the kinematic acceptance $\mathcal{A}$ of the event selection and the detection efficiency ε. The variables of interest for the sensitivity study of the $h\,(b\bar{b}) + E_T^{\rm miss}$

searches are

$$S_i = \frac{\sigma_i\left(pp \to h + E_T^{\text{miss}}\right)_{\text{2HDM+a}} \cdot \text{BR}\left(h \to b\bar{b}\right)_{\text{SM}} \cdot (\mathcal{A} \cdot \varepsilon)_i}{\sigma_i\left(pp \to h + E_T^{\text{miss}} \to b\bar{b} + E_T^{\text{miss}}\right)_{\text{obs}}}\,, \tag{8.1}$$

where $\sigma_i\left(pp \to h + E_T^{\text{miss}}\right)_{\text{2HDM+a}}$ is the partonic cross section of the 2HDM+a signal, the branching ratio of the SM Higgs boson is denoted by $\text{BR}\left(h \to b\bar{b}\right)_{\text{SM}} \simeq 58\%$ and $\sigma_i\left(pp \to h + E_T^{\text{miss}} \to b\bar{b} + E_T^{\text{miss}}\right)_{\text{obs}}$ represents the observed upper cross-section limit on $h + E_T^{\text{miss}}$ production with $h \to b\bar{b}$. The cross sections as well as the product $\mathcal{A} \cdot \varepsilon$ depend on the considered E_T^{miss} bin as indicated by the index i. A particular point in parameter space is expected to be excluded if the sum $S = \sum_i S_i$ of the individual sensitivities is larger than 1.

The results of our sensitivity study for the mono-Higgs signal in the $b\bar{b}$ decay channel are shown in Figure 21. The upper panel in the figure displays S as a function of M_a and M_A. One observes that the existing mono-Higgs searches allow to probe/exclude 2HDM+a scenarios with $M_A > M_h + M_a$ and sufficiently small M_a values, while they are only weakly sensitive to models where the mass hierarchy between A and a is reversed, i.e. $M_a > M_h + M_A$. Numerically, we find that for a light a with $M_a \simeq 100\,\text{GeV}$ one has $S > 1$ for all values $M_A \simeq [350, 1050]\,\text{GeV}$. Notice that in the parameter region $M_A > M_h + M_a$ the strong sensitivity of the search arises because the mono-Higgs signature is resonantly produced via $pp \to A \to ha \to h\chi\bar{\chi}$ — see the discussion in Section 6.1. The sensitivity of the search decreases for increasing (decreasing) M_A because the production rate of $pp \to A$ decreases (the Jacobian peak (6.2) is shifted to lower E_T^{miss} values). In the region $M_a > M_h + M_A$, the largest contribution to the $h + E_T^{\text{miss}}$ cross section again originates from resonant production, namely $pp \to a \to hA \to h\chi\bar{\chi}$. The resulting sensitivities are however much smaller compared to the case discussed before, because $\sigma\left(pp \to a\right)/\sigma\left(pp \to A\right) = \sin^2\theta/\cos^2\theta \simeq 1/7$, $\text{BR}\left(a \to Ah\right)/\text{BR}\left(A \to ah\right) < 1$ and $\text{BR}\left(A \to \chi\bar{\chi}\right)/\text{BR}\left(a \to \chi\bar{\chi}\right) \ll 1$ for the parameter choices made in (4.4).

The lower panel in Figure 21 shows the sensitivity S in the M_a–$\tan\beta$ plane fixing M_H, M_A and $M_{H^\pm}$ to (4.5). One observes that the existing mono-Higgs searches allow to exclude $\tan\beta \lesssim 3$ for $m_a \simeq 100\,\text{GeV}$ and $\tan\beta \lesssim 1$ for $m_a \lesssim 225\,\text{GeV}$. [Uli: Correct? Clarify!] From Figure 14 it is apparent that for such small values of $\tan\beta$, the $h + E_T^{\text{miss}}$ signal is dominantly produced through top-quark loops in gg-fusion. The corresponding production rate scales as $\sigma\left(gg \to A\right) \propto \cot^2\beta$, and as a result the sensitivity rapidly decreases for $\tan\beta > 1$. Notice that the decrease is to some extent counteracted by the fact that the Jacobian peak becomes more pronounced when $\tan\beta$ is increased (cf. the left panel in Figure 14). Another feature that is visible in the lower panel in Figure 21 is that at $\tan\beta \gtrsim 10$ the sensitivity of the mono-Higgs search starts to increase again, because the $b\bar{b}$-initiated production cross section behaves like $\sigma\left(b\bar{b} \to A\right) \propto \tan^2\beta$. Further plots of our mono-Higgs sensitivity study can be found in Appendix ??.

8.2 Mono-Z study

In the absence of model-independent limits on anomalous production of $Z + E_T^{\text{miss}}$ events, the expected sensitivity of the mono-Z search to the 2HDM+a model is estimated by

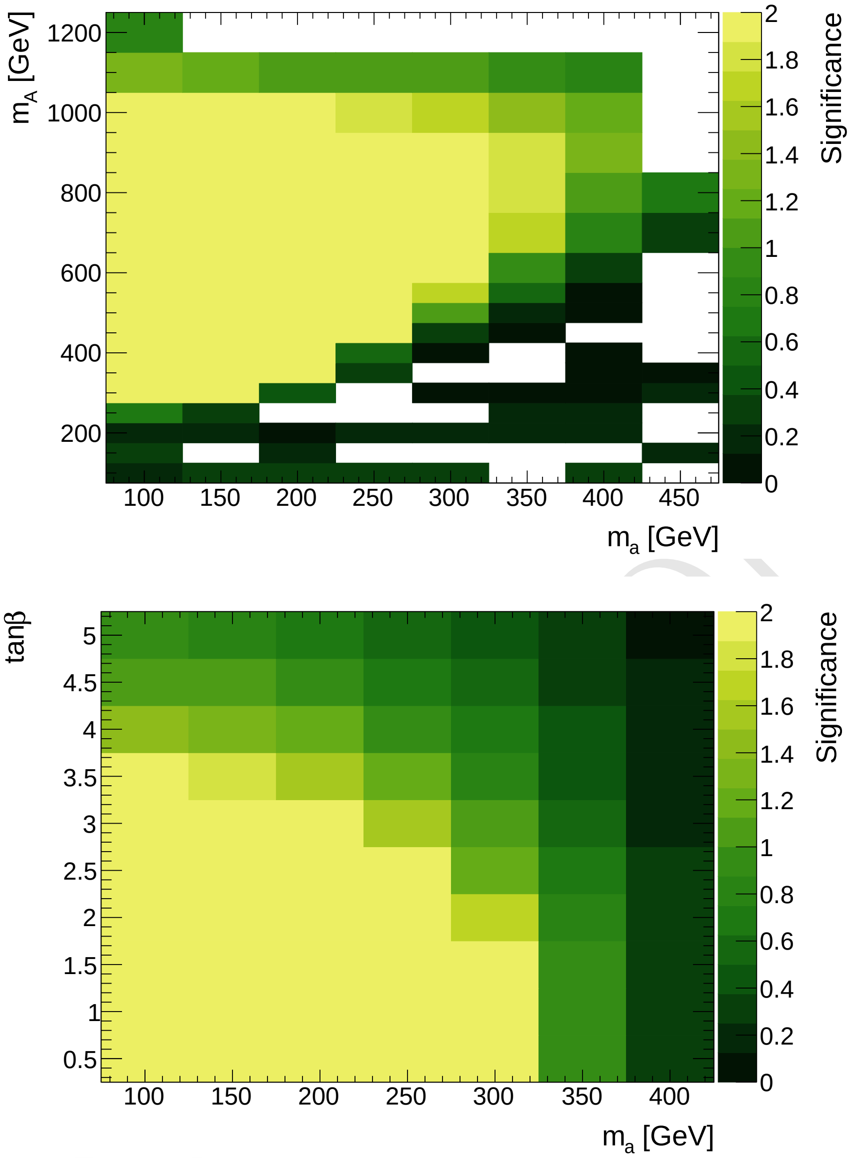

Figure 22: Estimated significance of the $Z + E_T^{\rm miss}$ signature in the $Z \to \ell^+\ell^-$ channel. The upper (lower) panel shows our results in the M_a–M_A (M_a–$\tan\beta$) plane. The choice of parameters resembles those made in Figure 21. Further details can be found in the text.

comparing the number of parton-level signal events to the number of expected background events. The published background predictions for $Z + E_T^{\rm miss}$ production followed by $Z \to \ell^+\ell^-$ [?] are used which correspond to $36\,{\rm fb}^{-1}$ of $13\,{\rm TeV}$ data. The selection cuts and $E_T^{\rm miss}$ binnings that are applied to the signal events resemble those employed in the ATLAS analysis [?]. A reconstruction efficiency of 75% is assumed for signal events, and a conservative background systematic uncertainty of 20% (10%) is taken for events with $E_T^{\rm miss} < 120\,{\rm GeV}$ ($E_T^{\rm miss} > 120\,{\rm GeV}$). Following the Asimov approximation, the significance $Z_{A,i}$ for individual bins i is calculated as a Poisson ratio of likelihoods modified to incorporate systematic uncertainties on the background. Explicitly one has [?]

$$Z_{A,i} = \sqrt{2\left((s+b)\ln\left[\frac{(s+b)\left(b+\sigma_b^2\right)}{b^2+(s+b)\,\sigma_b^2}\right] - \frac{b^2}{\sigma_b^2}\ln\left[1+\frac{\sigma_b^2 s}{b\left(b+\sigma_b^2\right)}\right]\right)}\,, \tag{8.2}$$

where s (b) represents the expected number of signal (background) events and σ_b denotes the standard deviation that characterises the systematic uncertainties of the background. The total significance Z_A is then defined by adding the individual $Z_{A,i}$ in quadrature. In this approximation, the ATLAS and CMS experiments are estimated to exclude regions with total significances of $Z_A > 2$.

The results of our sensitivity study for the mono-Z signature in the $\ell^+\ell^-$ channel are presented in Figure 22. The upper (lower) panel displays the total significance Z_A in the M_a–M_A (M_a–$\tan\beta$) plane. Comparing the obtained results to those depicted in Figure 21, one observes that for the parameter choices (4.4) the mono-Z and mono-Higgs searches allow to test quite similar parameter regions in the M_a–M_A plane. Numerically, we find that for $M_a \simeq 100\,\mathrm{GeV}$ the existing $Z+E_T^{\rm miss}$ searches are sensitive to 2HDM pseudoscalar masses in the range of $M_A \simeq [300, 1050]\,\mathrm{GeV}$. Notice that the mono-$Z$ sensitivity to lower values of M_A is slightly better than the one found in the mono-Higgs case. This enhanced sensitivity arises because for fixed M_A and M_a and given that $M_Z < M_h$ the endpoint $E_{T,\rm max}^{\rm miss}$ of the $E_T^{\rm miss}$ distribution in $Z + E_T^{\rm miss}$ production is always higher than that in the $h + E_T^{\rm miss}$ channel. In contrast, in the parameter region with $M_a > M_Z + M_A$ the sensitivity of the mono-Z signature is weaker than that of the mono-Higgs signal. This feature is readily understood by noticing that the $pp \to a \to ZH$ channel does not lead to a $E_T^{\rm miss}$ signature, since the scalar H does not decay invisibly in the 2HDM+a model. For $M_a > M_Z + M_A$ hence only non-resonant diagrams contribute to the $Z + E_T^{\rm miss}$ signature, and the sensitivity to such model realisations is consequently very weak.

In the lower panel of Figure 22 we plot the significance Z_A in the M_a–$\tan\beta$ plane for the choice (4.5). We see that present mono-Z searches are expected to exclude $\tan\beta \lesssim 3.5$ for $m_a \simeq 100\,\mathrm{GeV}$ and $\tan\beta \lesssim 1$ for $m_a \lesssim 325\,\mathrm{GeV}$. [Uli: Correct? Clarify!] The quoted exclusion limits are similar to the mono-Higgs case. We add that in models where the bottom-quark Yukawa coupling is $\tan\beta$ enhanced such as the type-II scenario studied here, $b\bar{b} \to Z + E_T^{\rm miss}$ production starts to become relevant for $\tan\beta \gtrsim 10$ [?]. Since only gg-fusion but not $b\bar{b}$-fusion production is included in our mono-Z simulations, only $\tan\beta$ values up to 5.5 are plotted in the lower panel of Figure 22. [Uli: In the view of Figure 15, I am not sure that even for $\tan\beta = \mathcal{O}(5)$ $b\bar{b}$-initiated production can be simply neglected!] Further details on our mono-Z sensitivity study are given in Appendix ??.

8.3 Sensitivity of other mono-X channels

The sensitivities of the LHC to the associated production of DM with a single top has been studied in the framework of the 2HDM+a model in [?]. This analysis assumes $300\,\mathrm{fb}^{-1}$ of data and finds that the $tX + E_T^{\rm miss}$ signatures complement the parameter space coverage of the mono-Higgs and mono-Z signals considered by us in detail. In fact, repeating the analysis of [?] using only $36\,\mathrm{fb}^{-1}$ of integrated luminosity, one finds that a combination of

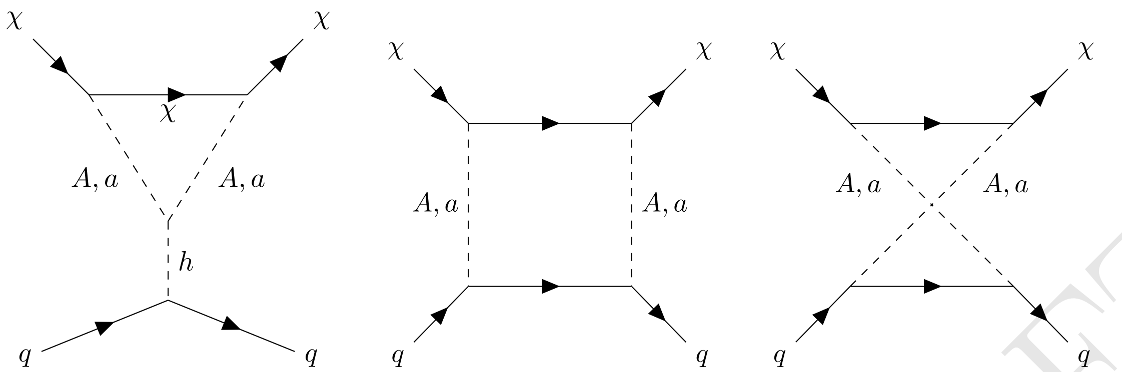

Figure 23: One-loop diagrams that lead to a SI DM-nucleon scattering cross section in the 2HDM+a model. Both triangle diagrams (left) as well as box graphs (middle and right) contribute in general. For further details consult the text.

the single-lepton and double-lepton channel allows to exclude values of $M_H = M_A = M_{H^\pm}$ in the range of around $[400, 1000]\,\mathrm{GeV}$ for $M_a = 150\,\mathrm{GeV}$, $\tan\beta < 1$ and $\sin\theta = 1/\sqrt{2}$. For $M_H = M_A = M_{H^\pm} = 700\,\mathrm{GeV}$ even a bound of $\tan\beta < 2$ can be set at 95% CL. While a direct comparison with the limits obtained in the mono-Higgs and mono-Z case is not possible due to the different value of $\sin\theta$ used in Sections 8.1 and 8.2, we note that the $\tan\beta$ values probed by all three searches lie in the same ballpark. Another feature that is worth recalling is that the $h + E_T^{\mathrm{miss}}$, $Z + E_T^{\mathrm{miss}}$ and $tW + E_T^{\mathrm{miss}}$ signature can be resonantly enhanced through A, H and $H^\pm$ exchange in the 2HDM+a model (see Figure 6). Observing correlated deviations in all three channels might hence allow to determine the complete non-SM Higgs spectrum.

Sensitivity studies of the $t\bar{t} + E_T^{\mathrm{miss}}$ and $j + E_T^{\mathrm{miss}}$ channels in the 2HDM+a have been performed in [**?**]. The results presented in that work imply that for the benchmark parameter choices (4.4), the latest $t\bar{t} + E_T^{\mathrm{miss}}$ and mono-jet searches that are based on $36\,\mathrm{fb}^{-1}$ of 13 TeV data have only a very weak sensitivity to the parameter space shown in Figures 21 and 22. Given the limited sensitivity of the $t\bar{t} + E_T^{\mathrm{miss}}$ and $j + E_T^{\mathrm{miss}}$ modes, we leave detailed sensitivity studies for these channels for future work. The $b\bar{b} + E_T^{\mathrm{miss}}$ channel is also not considered here due to the same reason. Notice however that a reinterpretion of existing $t\bar{t} + E_T^{\mathrm{miss}}$, $b\bar{b} + E_T^{\mathrm{miss}}$ and $j + E_T^{\mathrm{miss}}$ results is straightforward by using the general rescaling strategy discussed in Appendix A.

9 Constraints from other DM experiments

In this section we briefly discuss the constraints that direct and indirect detection DM experiments set on the parameter space of the 2HDM+a model. We will illustrate both the existing constraints as well as show future projections.

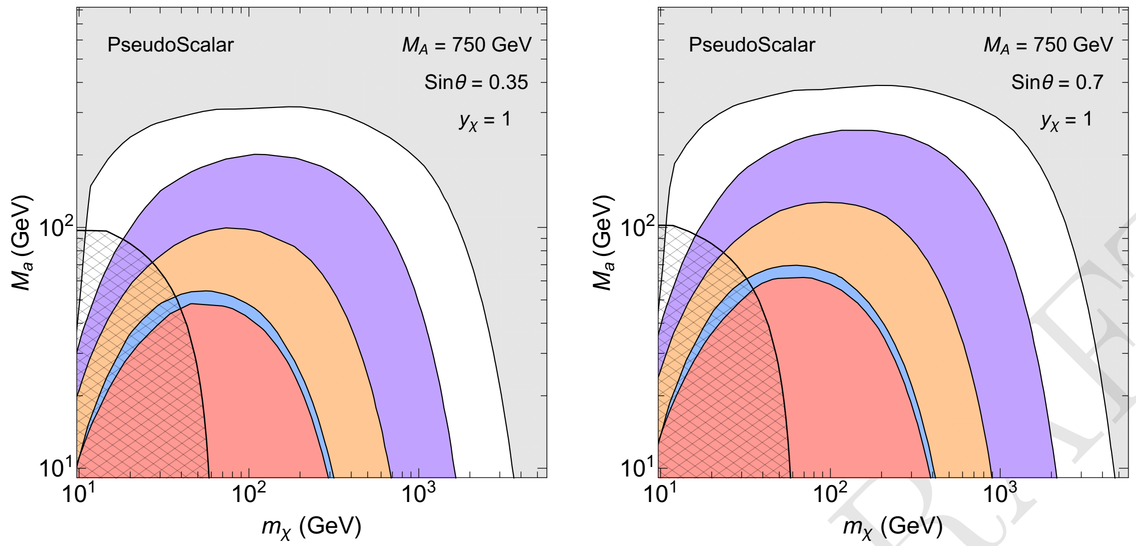

Figure 24: DD exclusions in the 2HDM+a model as function of m_χ and M_a. The constraints from LUX (red) [?], XENON1T (blue) [?] and the projections from XENON1T (orange) and XENONnT (purple) [?] are shown. The grey shaded area is not accessible to ordinary DD experiments due to the presence of the neutrino background [?], while the black hatched regions are excluded by the LHC bounds on invisible Higgs decays. In the left (right) panel the parameters $\sin\theta = 0.35$ ($\sin\theta = 0.7$), $M_A = 750\,\text{GeV}$ and $y_\chi = 1$ are employed. [Uli: Are these plots $\tan\beta$ independent? They contain only the triangles? Is this a type-II model? What has been chosen for the λ_i parameters? Fix notation?]

9.1 Direct detection

The constraints from direct detection (DD) for pseudoscalar mediators are generally suppressed at tree level, so that the dominant contributions arise from one-loop Feynman diagrams [? ? ?]. In the case of the 2HDM+a model a spin-independent (SI) DM-nucleon scattering cross section is generated by the graphs shown in Figure 23. Notice that the triangle diagram shown on the left-hand side is proportional to a single power the Yukawa coupling y_q, while the box diagrams that are displayed in the middle and on the right of the figure are proportional to y_q^3. It follows that the triangle graph generically provides the dominant contribution to the SI DM-nucleon scattering cross section. The only exceptions are models that feature a Yukawa sector with $\tan\beta$-enhanced down-type Yukawa couplings such as type-II models, where the box diagrams can be numerically important if $\tan\beta \gtrsim 50$. This has first been pointed out in [?]. Unlike the box graphs the triangle diagram does not depend on the Yukawa sector of the 2HDM+a model [? ?].

The constraints that DD experiments can or may set on the parameter space of the 2HDM+a model are presented in Figure 24. In the left (right) panel the parameters $\sin\theta = 0.35$ ($\sin\theta = 0.7$), $M_A = 750\,\text{GeV}$ and $y_\chi = 1$ are employed. For $\sin\theta = 0.35$,

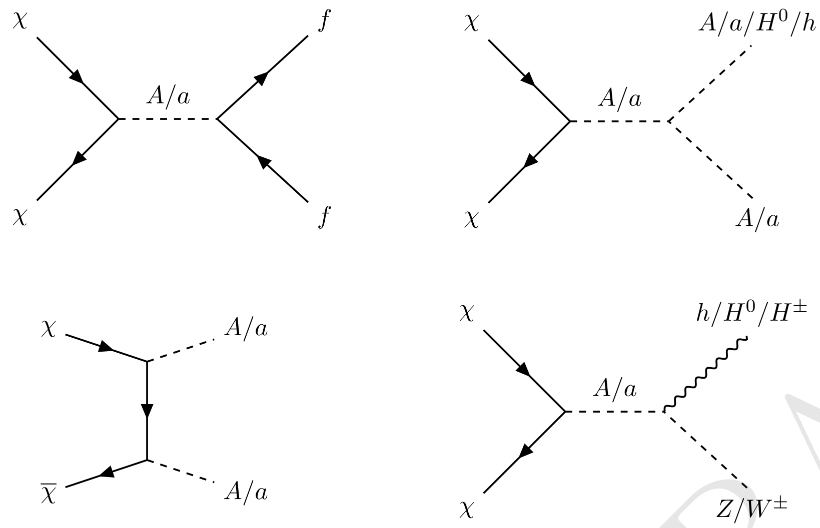

Figure 25: Tree-level annihilation diagrams of DM in the 2HDM+a model. Annihilations into pairs of SM fermions (f), Higgses (h, H, A, a) and a Higgs and a EW gauge boson (HZ and $H^\pm W^\pm$) are possible in the alignment limit. [Uli: Fix notation? Why do have some χ's are bar others not?]

current limits from LUX (red) [?] and XENON1T (blue) [?] are able to exclude the portion of parameter space with $m_\chi \in [20, 200]$ GeV and $M_a \lesssim 40$ GeV. Projected limits from XENON1T (orange) and XENONn (purple) [?] are expected to expand the excluded region to $m_\chi \in [10, 1000]$ GeV and $M_a \lesssim 150$ GeV. In the case $\sin\theta = 0.7$, the obtained limits are slightly better because of the larger mixing angle. For comparison also the regions in the m_χ–M_a plane excluded by the present LHC bounds on invisible Higgs decays — see Section 4 and [?] — are shown as black hatched regions. From the results displayed in Figure 24 is is also evident that present and future DD experiments cannot probe the benchmarks (4.4) since these employ $m_\chi = 10$ GeV. In fact, the sensitivity of DD is complementary to that of the mono-X searches because the former constraints are strongest for $m_a < m_\chi/2$ while the latter searches provide the best exclusions for $m_a > m_\chi/2$.

9.2 Indirect detection

Due to the large number of interactions that the mediators A, a have with SM or 2HDM states, the indirect detection (ID) signals in the 2HDM+a model are quite complex. In fact, in the pure alignment limit $\cos(\beta - \alpha) = 0$, the possible annhihilation channels of DM are $f\bar{f}$, hA, HA, HZ, $H^\pm W^\mp$, ha, Ha, AA, aa and Aa. Here f denotes all SM fermions that are kinematically accessible for a given DM mass, i.e. those fermions with $m_f < m_\chi$. Example of relevant diagrams are shown in Figure 25. Since the SM gauge bosons and the Higgs states decay further into pairs of SM fermions, the final states resulting from the $\chi\bar{\chi}$ annihilation can contain either two or four SM particles.

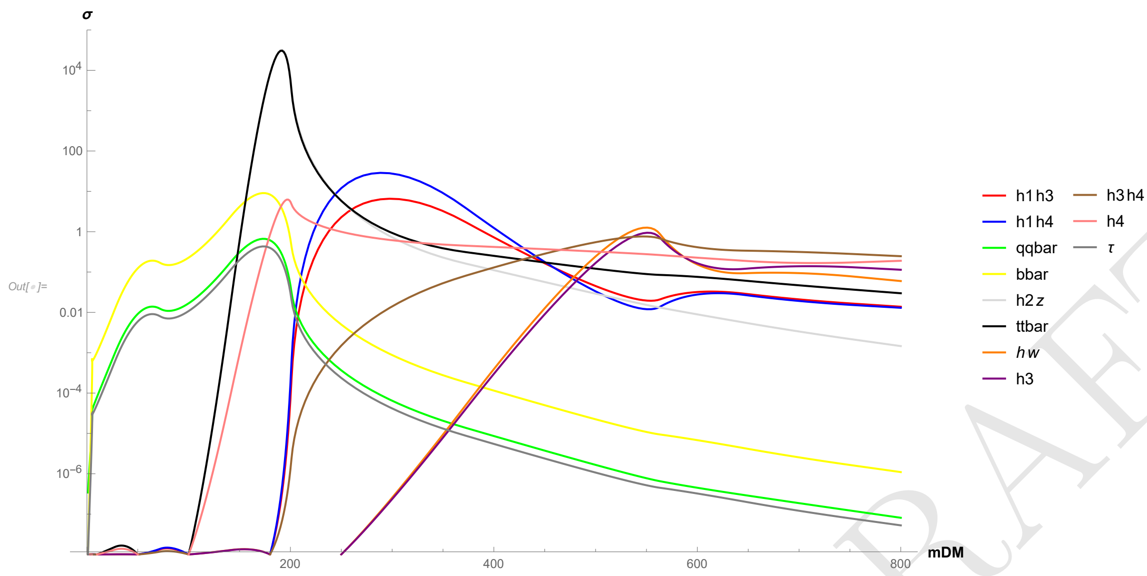

Figure 26: A Plot of the leading Dark Matter partial annihilation cross sections, in picobarns, to various final state particle pairs, vs Dark Matter Mass (GeV). The curves include annihilation rates into fermions, pairs of Higgs sector particles, and Vector Boson-Higgs pairs.

[Uli: The text below has to be changed!]

In short, Dark Matter can annihilate into many final state particle pairs, and an increasing number of distinct event topologies become kinematically accessible with increasing Dark Matter mass. Not only can the DM annihilate to various pairs of Standard Model particles, but DM may also annihilate into single SM gauge boson produced in association with an unstable Higgs sector particle, or into two Higgs sector particles. In turn, the Higgs sector particles will decay to pairs of SM particles, therefore the final states of DM annihilation may contain 2, 3 or 4 SM particles and the content of the dominant annihilation channel will not only depend on the Higgs sector parameters and Dark Matter mass. When fixing the coupling parameters and varying the DM mass, one can see the changes in the dominant DM annihilation channels as the different energy thresholds are crossed, as shown in this section.

To illustrate the complexity of the DM annihilation channels which contribute to indirect detection, Figure 26 shows the total DM annihilation rate vs Dark Matter mass for specific benchmark values of the Higgs sector parameters. The cross sections were calculated using the Madgraph version of the model available on the DMWG repository **??** and the MadDM plugin[**?**].

As the DM mass in increased the dominant annihilation channel varies greatly. For light Dark Matter masses, under about 150 GeV, the annihilation rate is dominated by b-quark pairs, as they are the kinematically accessible particles that have the largest Yukawa coupling to the Higgs=sector mediator. This situation resembles the light Higgs boson decay rates, dominated by bottom quarks. A new annihilation channel into a Higgs and Z boson opens when the threshold $m_{DM} \to m_h + m_Z$ is crossed. Next, the $m_{DM} \to m_t$, where the di-top channel opens and contributes significantly to the annihilation rate. The next threshold to be crossed is $2m_{DM} \to m_a + m_h$, where the light pseudo-scalar will decay to bottom quarks. The event is thus likely $2m_{DM} > 4b$, however the momentum distribution between the two pairs of bottoms will be asymmetric. It is expected that the total annihilation rate into this channel is appreciable since there is a large coupling between the Higgs and the pseudoscalar which also involves mass insertion. This type of event topology, $DMDM \to X + SM$, where X is a decaying hidden sector particle, has not been extensively studied on its own. Next, the threshold $2m_{DM} > m_V + m_H$ is crossed, where V is the mass of a heavy vector boson, and H is a heavier Higgs sector field. Along with all of this, modes will significantly contribute where DM annihilates to pairs of Higgs sector fields. The most important, and lowest threshold is $m_{DM} \to m_a$, where the annihilation channel into two pseudoscalars is open. There are also thresholds where DM annihilates to any pair of heavy (or one heavy and one light) Higgs sector field.

A few general notes are in order here. First, the effect of the new annihilation channels opening as thresholds are crossed may also be witnessed in figure 26 which charts the relic density as a function of DM mass for fixed values of the Higgs-sector parameters. One can see, for example, the effect of the di-top channel turning on as the overall annihilation rate is enhanced and the relic density drops. A similar powerful effect is observed as the threshold $2m_{DM} \to m_a + m_h$ is crossed. The significant drop in relic density at this threshold demonstrates that this is an important annihilation channel which can compete or even dominate the list of partial annihilation rates. The annihilation rate is enhanced as the resonance thresholds $2m_{DM} = m_a, m_A$ are crossed, which will lead to stronger constraints from total photon flux measurements from indirect detection (ID) experiments.

We note that indirect detection constraints for models of the complexity of kinematics displayed here not yet been well studied. In much of parameter space, the annihilation cross sections are not simply dominated by a single final state channel, several distinct channels often have significant contributions. Since many channels will contribute to over-all photon flux and limits obtained from flux observation will require that these distinct spectra using a method similar to reference [**? ?**] to combine channels. The total photon flux expected from DM annihilations will be

$$\Phi_\gamma = \frac{1}{4\pi} \sum_f \frac{\langle \sigma_v \rangle}{2m_\chi^2} \int_{E_{min}}^{E_{\max}} \left(\frac{dN_\gamma}{dE_\gamma} \right)_f dE_\gamma J \tag{9.1}$$

where the J-factor ($\mathrm{GeV}^2\mathrm{cm}^{-5}$) is the line of sight integral of the DM density ρ, integrated over a solid angle: $\Delta\Omega$, m_χ is the Dark Matter mass, and we must sum over all accessible partial annihilation rates $\langle \sigma v \rangle_f$, where f specifies the distinct final state. These predictions of total integrated flux may then be compared to observational measurements, for example of dwarf galaxies or the galactic center, which may constrain the partial annihilation rates and thus provide limits on the model parameters. In reference [?], complex models with several annihilation channels were constrained using the Fermi dwarf galaxy data, where the observations of each dwarf galaxy was stacked in a joint-likelihood analysis. Such a procedure would be optimal for setting limits on this model from existing observational data. Below, we briefly describe the effect of various mass thresholds on the admixture of partial annihilation rates in our model.

The annihilations which involve the unstable Higgs fields will have more complicated kinematics than simple DM annihilation to 2 SM particles. Some work has been done regarding shifts in the annihilation spectrum resulting a very symmetric process where DM pairs annihilate to 2 or more identical heavy states that then decay to pairs of SM particles [?]. Our model presents this as a possible annihilation process, along with others which have not yet been analysed. These include the asymmetric process where 2 decaying Higgs sector particles of differing masses are produced and other asymmetric processes where light SM particle is produced in association with a heavier Higgs sector particle. The full parameter space of this model presents a wide area of admixtures of annihilation channels, and thus many possibilities for total integrates photon spectra. We see that this type of 2HDM is quite complex, both in the number of annihilation channels and in kinematics as well.

10 DM relic density

In this section, we check the consistency of the 2HDM+a model as a function of the parameters chosen for the scans with the measured DM relic density, according to the standard thermal relic "freeze-out" scenario. This exercise requires the following assumptions, already detailed in [?]. First, the DM annihilation cross section receives only contributions from the interactions of the 2HDM+a model, while possible additional degrees of freedom and couplings not included in the model are ignored. Second, the DM number density in the Universe today is entirely determined by the DM annihilation cross section predicted by the 2HDM+a model. In particular, no additional mechanisms exist that enhance or deplete the DM relic density. It is important to realise that if one or both of these assumptions are violated there is no strict correlation between the relic density and the strength of mono-X signals. For instance, if DM is overproduced, the relic density can be reduced if the DM has large annihilation cross sections to new hidden sector states. These states might however not be directly accessible at LHC energies. Conversely, the correct DM relic density can still be obtained if the DM is underproduced. For instance, if the hidden sector carries an particle-antiparticle asymmetry (similar to the baryon asymmetry) then this necessarily leads to a larger relic density compared to the conventional freeze-out picture.

10.1 Calculation

The Feynman diagrams of the annihilation processes taken into account in the calculation of the DM relic density in the 2HDM+a model are shown in Figure 25. Generally, the

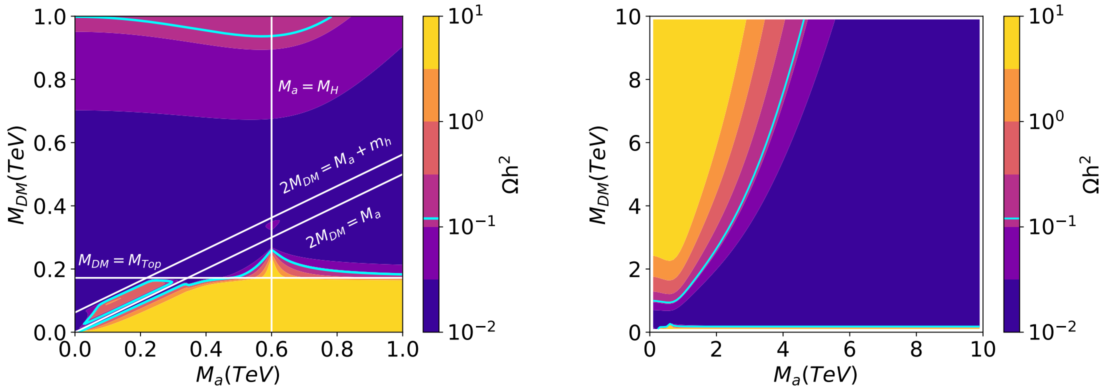

Figure 27: Predicted DM relic density for a two-dimensional scan of M_a and m_χ. The other parameters remain fixed at $M_H = M_A = M_{H^\pm} = 600\,\text{GeV}$ and $\tan\beta = 1$, as well as the benchmark choices given in (4.4). The color scale indicates the DM relic density, the cyan solid line shows the observed value of $\Omega h^2 = 0.12$. The color scale is truncated at its ends, i.e. values larger than the maximum or smaller than the minimum are shown in the same color as the maximum/minimum. While the left panel focuses on the mass region relevant to collider searches, the right panel shows the development of the DM relic density for a larger mass region. [Uli: Fix notation?]

annihilation proceeds via single or double s-channel exchange of the pseudoscalars A and a with subsequent decays. The `MadDM` [? ?] plugin for `MadGraph5_aMC@NLO` [?] is used to calculate the present-day DM relic density. Since `MadDM` uses only $2 \to 2$ scattering diagrams [Uli: Correct?], contributions from off-shell pseudoscalars can only be taken into account for the case of single s-channel mediation with direct decay of the pseudoscalars to SM fermions. If the pseudoscalars instead decays to other bosons or if the annihilation proceeds through double s-channel diagrams, the outgoing bosons are taken to be on-shell and their decays are not simulated. All tree-level annihilation processes are considered, and the Yukawa couplings of all fermions are taken to be non-zero.

10.2 Scan results

The DM relic density is shown in the M_a–m_χ plane in the two panels of Figure 27. The parameters not indicated in the plots are fixed to $M_H = M_A = M_{H^\pm} = 600\,\text{GeV}$, $\tan\beta = 1$ and the choices introduced in (4.4). One see from the left panel that for values of m_χ below the mass of the top quark, DM is mostly overabundant. In this regime, annihilation to quarks is suppressed by the small Yukawa couplings of the light fermions. The observed DM relic density can only be achieved for $m_\chi \simeq M_a/2$, where annihilation is resonantly enhanced, or for $m_\chi \simeq (M_a + M_h)/2$, close to the threshold for the $\chi\chi \to ha$ process. Above the top threshold, annihilation into fermions becomes very efficient and DM is underabundant. As m_χ increases further, annihilation via single s-channel diagrams is more and more suppressed and the observed DM relic density can again be reproduced. At low values of M_a this happens for $m_\chi \simeq 1\,\text{TeV}$ as can be nicely seen from the plot depicted

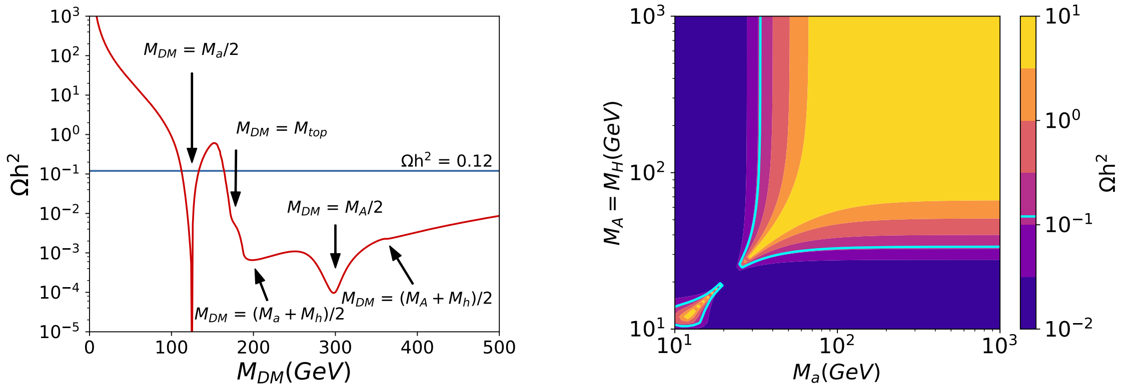

Figure 28: Left: DM relic density in the 2HDM+a model as a function of m_χ. The shown predictions are obtained for $M_H = M_A = M_{H^\pm} = 600\,\text{GeV}$, $M_a = 250\,\text{GeV}$, $\tan\beta = 1$ and the benchmark choices (4.4). See text for further details. Right: Predicted DM relic density for the 2HDM+a model in the M_a-M_a plane. A common mass $M_H = M_A = M_{H^\pm}$ is used and (4.4) is employed. The colour coding resembles that of Figure 27.

on the left-hand side of Figure 27. For the sake of completeness, we show in the right panel of the latter figure also the two branches of solutions for masses up to 10 TeV.

The dependence of the DM relic density on the choice of the DM mass m_χ is further explored on the left-hand side of Figure 28. The red curve corresponds to the choices $M_H = M_A = M_{H^\pm} = 600\,\text{GeV}$, $M_a = 250\,\text{GeV}$, $\tan\beta = 1$ and (4.4). The shown result confirms the presence of the previously discussed regions of resonant enhancement and kinematic boundaries. Overall, the behaviour is dominated by the low-m_χ suppression of the annihilation cross section, the resonant enhancement at $m_\chi = M_a/2$ and the kinematic top thresholds. Other effects, such as the resonant enhancement of $\chi\chi \to A$ annihilation are present, but only have small effects.

The DM relic density values for the M_a–M_A scan adopting the benchmark parameters (4.4) are shown in the right panel of Figure 28. From the plot it is evident that the regions where the 2HDM+a model predicts a DM relic density compatible with the measured value $\Omega h^2 = 0.12$ are located either at $M_a < 30\,\text{GeV}$ or at $M_A = M_H = M_{H^\pm} < 30\,\text{GeV}$. As explained in Section 4 the first option is excluded by the LHC bounds on invisible Higgs decays, while the second possibility is ruled out directly by LEP and LHC searches for charged Higgses and indirectly by flavour physics. This means that the benchmark (4.4) employed in this whitepaper cannot give rise to the correct DM relic density as it generically predicts $\Omega h^2 \gg 0.12$. Since the cosmological production of DM is largely driven by the choice of m_χ it is however possible to tune the DM mass such that the correct DM relic density is obtained in scenarios (4.4) with $m_\chi \neq 10\,\text{GeV}$. For instance, by choosing the DM mass to be slightly below the a threshold, i.e. $m_\chi = M_a/2$, one can attain $\Omega h^2 \lesssim 0.12$ (see the left panel in Figure 28). Given that both the total cross sections and the kinematics distributions of the mono-X signatures are largely insensitive to the precise choice of m_χ as long as one has $m_\chi < M_a/2$ (cf. Figure 16), our sensitivity studies performed in

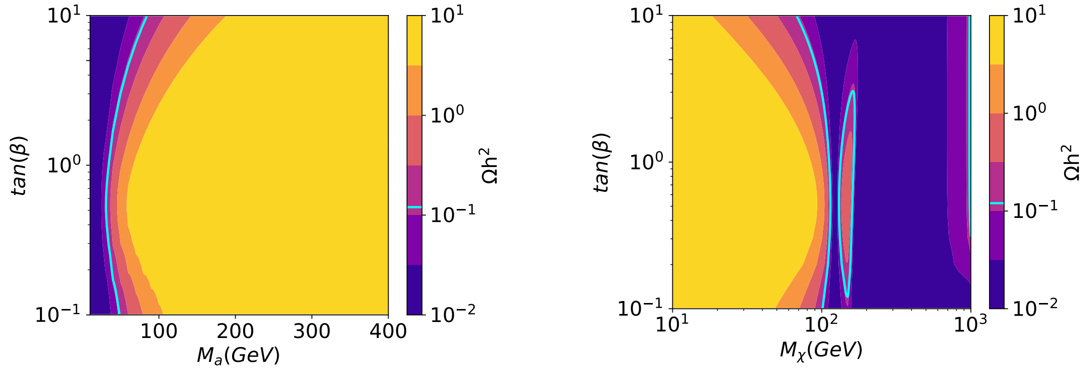

Figure 29: Predicted DM relic density in the 2HDM+a model in the $M_a-\tan\beta$ (left panel) and $m_\chi-\tan\beta$ (right panel) plane, respectively. In the left (right) panel, $m_\chi = 10\,\text{GeV}$ ($m_a = 250\,\text{GeV}$) is employed as well as (4.4) with $M_H = M_A = M_{H^\pm} = 600\,\text{GeV}$. The color coding is identical to Figure 27.

Section 8 apply to first approximation also to scenarios a la (4.4) where the measured DM relic density is obtained by tuning $m_\chi \simeq M_a/2$.

In Figure 29 we display $\tan\beta$ scans as a function of M_a (left panel) and m_χ (right panel). Both panels show that the values of M_a (m_χ) for which $\Omega h^2 = 0.12$ do not depend strongly on the precise choice of $\tan\beta$. From the left plot one see that for a choice of $\tan\beta \simeq 0.6$ the relic density becomes maximal and steadily decreases for larger and smaller values of $\tan\beta$. Notice that in the case of the $m_\chi-\tan\beta$ scan, the reduction of the DM relic density at $\tan\beta \simeq 0.1$ and $\tan\beta \simeq 3$ leads to the disappearance of the overabundant island around $m_\chi \simeq M_a/2$.

11 Proposed parameter scans

The discussion of the theoretical motivations presented in Section 4 together with our explicit studies in Sections 6, 7, 8, 9 and 10 suggest certain benchmarks for the parameters given in (3.7). In this section, we describe how the parameter space of the 2HDM+a model can be effectively explored through two-dimensional (2D) and one-dimensional (1D) scans of five input parameters: a common 2HDM heavy Higgs mass $M_H = M_A = M_{H^\pm}$, the pseudoscalar mass M_a, the mixing angle $\sin\theta$, the ratio $\tan\beta$ of VEVs of the two 2HDM Higgs doublets and the DM mass m_χ. The benchmark scenarios proposed here have been agreed within the DMWG. They are not meant to provide an exhaustive scan of the entire parameter space of the 2HDM+a model, but are supposed to highlight many of the features that are special in the model and showcase the complementarity of the various signatures.

Scan in the M_a, $M_H = M_A = M_{H^\pm}$ plane

The main 2D parameter grid proposed to explore the 2HDM+a model with LHC data spans the combination of the pseudoscalar mass M_a and a common heavy 2HDM Higgs mass $M_H = M_A = M_{H^\pm}$. The proposed values of the remaining 2HDM+a parameters

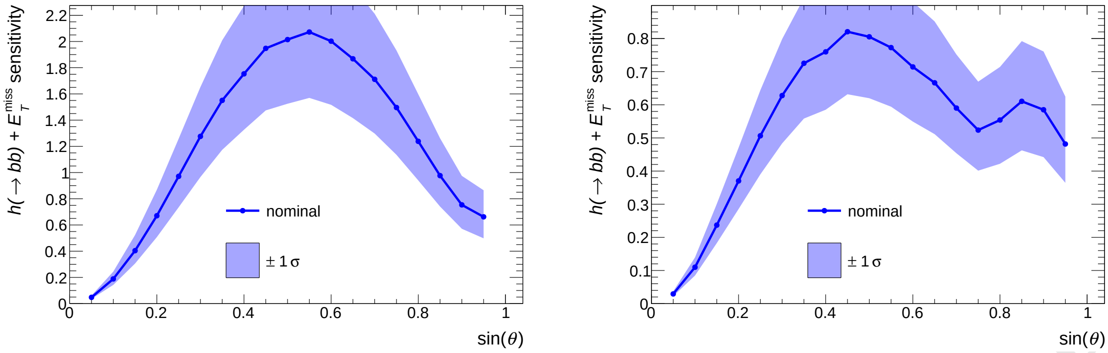

Figure 30: Estimated sensitivities of the $h\,(b\bar{b}) + E_T^{\rm miss}$ channel as a function of $\sin\theta$. The left (right) panel shows our results for $M_H = M_A = M_{H^\pm} = 600\,\text{GeV}$ and $M_a = 200\,\text{GeV}$ ($M_H = M_A = M_{H^\pm} = 1000\,\text{GeV}$ and $M_a = 350\,\text{GeV}$). The remaining parameters are set equal to (4.4). The sensitivities (points and curves), defined as the sum (8.1) over $E_T^{\rm miss}$ bins, as well as the uncertainty on the sensitivities (shaded bandes) are based on the limits from [**?**] and the uncertainties described therein. Bins with no content have a negligible sensitivity. [Uli: Use the same notation etc. for the plots in Figures 21, 22 and 30!]

are given in (4.4). Two example scans in the suggested mass-mass plane are given in the upper panels of Figures 21 and 22. These plots show the results of our sensitivity studies in the $h\,(b\bar{b}) + E_T^{\rm miss}$ and $Z\,(\ell^+\ell^-) + E_T^{\rm miss}$ channel, respectively, and are based on $36\,\text{fb}^{-1}$ of 13 TeV LHC data. From the figures it is evident that in the benchmark scenario (4.4), one can already probe a masses up to almost 350 GeV and common heavy 2HDM Higgs masses in the range of around $[300, 1000]\,\text{GeV}$ with existing data. By interpreting other mono-X channels such as $tW + E_T^{\rm miss}$, $t\bar{t} + E_T^{\rm miss}$ and $j + E_T^{\rm miss}$ (cf. Section 6) as well as non-$E_T^{\rm miss}$ searches for final states like $\tau^+\tau^-$, tb and $t\bar{t}t\bar{t}$ (cf. Section 7) in this plane will allow to nicely illustrate the complementary of the different search strategies for the spin-0 2HDM+a states at the LHC. Furthermore, combinations of the results of different searches can be done consistently for (4.4) and are expected to cover more parameter space than considering one signature at a time.

Scan in the $M_a - \tan\beta$ plane

A 2D scan in the $M_a - \tan\beta$ plane with the common heavy 2HDM Higgs masses fixed to $M_H = M_A = M_{H^\pm} = 600\,\text{GeV}$ is proposed. The remaining parameters should be chosen as in (4.4). Two example of such a scan can be found in the lower panels of Figures 21 and 22. From the two plots one sees that with $36\,\text{fb}^{-1}$ of 13 TeV LHC data, mono-Higgs and mono-Z searches are already sensitive to $\tan\beta = \mathcal{O}(1)$ values for a masses up to around 300 GeV. Other mono-X searches like $t\bar{t} + E_T^{\rm miss}$ and $j + E_T^{\rm miss}$ are at present only sensitive to $\tan\beta \lesssim 0.5$, which emphasises the special role that resonant $E_T^{\rm miss}$ signatures such as $h + E_T^{\rm miss}$, $Z + E_T^{\rm miss}$ and $tW + E_T^{\rm miss}$ play in the 2HDM+a model (see Section 6.1). Like the mass-mass plane discussed before also the $M_a - \tan\beta$ plane offers a nice way to compare and to contrast the LHC reach of $E_T^{\rm miss}$ and non-$E_T^{\rm miss}$ searches in the 2HDM+a context.

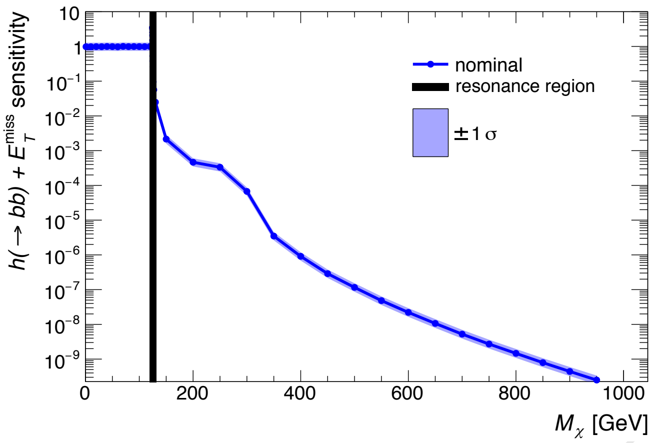

Figure 31: Estimated sensitivities of the $h\,(b\bar{b}) + E_T^{\rm miss}$ channel as a function of m_χ. The shown results correspond to $M_H = M_A = M_{H^\pm} = 600\,\text{GeV}$, $M_a = 250\,\text{GeV}$ and the parameter choices made in (4.4). The colour coding resembles that used in Figure 30. [Uli: Fix notion? I would also strongly suggest to remove the points at $m_\chi = M_a/2$ by hand! A double-logarithmic plot and restricting the x-axis to $[1, 500]\,\text{GeV}$ would also be nice!]

Scans in $\sin\theta$

Two 1D scans in $\sin\theta$ are also proposed, one with $M_H = M_A = M_{H^\pm} = 600\,\text{GeV}$ and $M_a = 200\,\text{GeV}$ and a second one with $M_H = M_A = M_{H^\pm} = 1000\,\text{GeV}$ and $M_a = 350\,\text{GeV}$. In both scans, the remaining parameters should be set equal to (4.4). In Figure 30 we show the estimated sensitivities of the mono-Higgs signal with $h \to b\bar{b}$ (see Section 8.1 for further details on the sensitivity $h\,(b\bar{b}) + E_T^{\rm miss}$ study) that derive from the ATLAS search [**?**] for the two recommended $\sin\theta$ benchmarks. We recommend the scans in $\sin\theta$, because they will in particular allow for a further comparison of the sensitivities of the mono-Higgs and mono-Z searches given that these two channels have a different $\sin\theta$ dependence (cf. Figure 13). We add that for the two proposed scans only values of $\sin\theta < 0.75$ and $\sin\theta < 0.45$ will lead to a scalar potential that satisfies the BFB conditions. This follows from the inequality (4.2). [Uli: We should discuss if these benchmarks are really the best ones?!]

Scan in m_χ

In order to make contact to DD and ID detection as well as the DM relic density calculation, which are strongly dependent on the choice of the DM mass, we also recommend to perform 1D scans in m_χ spanning from $1\,\text{GeV}$ to $500\,\text{GeV}$. The Higgs masses should be taken as $M_H = M_A = M_{H^\pm} = 600\,\text{GeV}$ and $M_a = 250\,\text{GeV}$ [Uli: Why $M_a = 250\,\text{GeV}$ and not as before $M_a = 200\,\text{GeV}$?] in these scans and the other 2HDM+a parameters set to (4.4). Figure 31 shows the results of such a scan for the case of the expected sensitivity of the $h\,(b\bar{b}) + E_T^{\rm miss}$ channel following from [**?**]. Notice that with the present data set the used mono-X search has sensitivity to DM masses up to around $m_\chi \simeq M_a/2 = 125\,\text{GeV}$. For DM masses such that $m_\chi \simeq M_a/2$ the observed DM relic density can however also be obtained (cf. Section 10). Such fine-tuned 2HDM+a scenarios are hence in agreement with cosmological observations (assuming a standard freeze-out picture) and can be probed/excluded with the help of the LHC.

While in all our scan recommendations we have employed a common 2HDM heavy Higgs mass $M_H = M_A = M_{H^\pm}$, in future 2HDM+a interpretations of LHC data one may also want to consider cases with $M_H \neq M_A$, since having a mass splitting between the H, A and $H^\pm$ can lead to interesting effects in the mono-Higgs and mono-Z searches (see Figure 12) as well as the $t\bar{t}Z$ and tbW final states (cf. the discussion in Section 7.3). [Uli: I have added the last paragraph to the discussion, but it could also be dropped. Its up for discussion!]

Acknowledgments

Ulrich Haisch acknowledges the continued hospitality and support of the CERN Theoretical Physics Department.

A Recasting procedure

In this appendix we discuss a general strategy that can be used to reinterpretion existing $t\bar{t}+E_T^{\text{miss}}$, $b\bar{b}+E_T^{\text{miss}}$ and $j+E_T^{\text{miss}}$ results obtained in the DMF pseudoscalar model in terms of the 2HDM+a model. Example diagrams that lead to these mono-X signatures in the 2HDM+a model are displayed Figure 10. Notice that only graphs involving the exchange of an a are depicted in this figure but similar diagrams with an A are not explicitly shown.

The relevance of the contributions from both the a and A in the 2HDM+a model can be nicely demonstrated by considering the invariant mass $m_{\chi\bar{\chi}}$ of the $\chi\bar{\chi}$ system. Examples of $m_{\chi\bar{\chi}}$ distributions in $t\bar{t}+E_T^{\text{miss}}$ production are shown in the left panel of Figure 32. The brown (magenta) histogram corresponds to the prediction in the DMF pseudoscalar model assuming a mediator mass of $M_a = 100\,\text{GeV}$ ($M_a = 600\,\text{GeV}$), while the cyan histogram illustrates the result in the 2HDM+a model for the choices $M_a = 100\,\text{GeV}$, $M_H = M_A = M_{H^\pm} = 600\,\text{GeV}$, $\sin\theta = 0.7071$ and $\tan\beta = 1$. One observes that the predictions obtained in the DMF pseudoscalar model both show a single Breit-Wigner peak at $m_{\chi\bar{\chi}} = M_a$, which corresponds to the on-shell production of the mediator a that subsequently decays to a pair of DM particles. The 2HDM+a result instead features two mass peaks, one at $m_{\chi\bar{\chi}} = M_a$ and another one at $m_{\chi\bar{\chi}} = M_A$, because both pseudoscalars can be produced on-shell and then decay invisibly via either $a \to \chi\bar{\chi}$ or $A \to \chi\bar{\chi}$.

The above discussion suggests that once the contributions from a and A production are separated, $t\bar{t}+E_T^{\text{miss}}$, $b\bar{b}+E_T^{\text{miss}}$ and $j+E_T^{\text{miss}}$ results obtained in the DMF pseudoscalar model can be mapped into the 2HDM+a parameter space. In practice, the remapping is achieved by calculating the selection acceptances $\mathcal{A}_{\text{DMF}}(M_a)$ and $\mathcal{A}_{\text{DMF}}(M_A)$ in the DMF pseudoscalar model and the respective cross sections $\sigma_{a,\text{DMF}}$ and $\sigma_{A,\text{DMF}}$. The acceptance $\mathcal{A}_{\text{2HDM+a}}(M_a, M_A)$ in the 2HDM+a model is then obtained by computing the

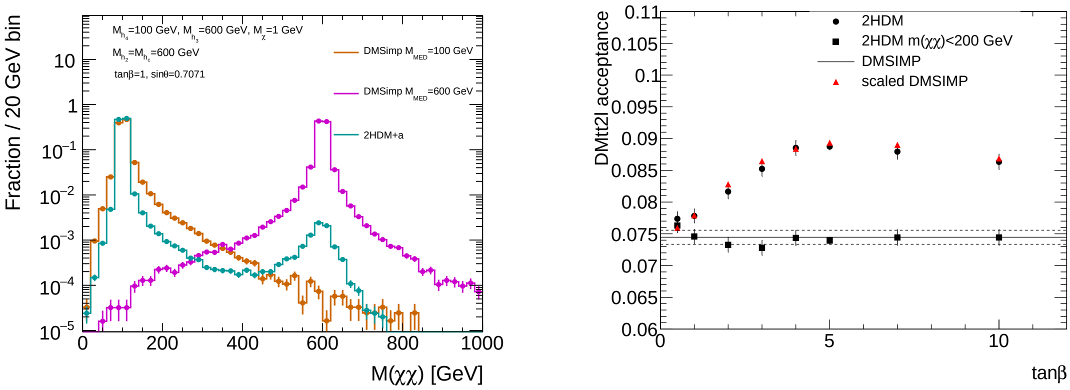

Figure 32: Left: Invariant mass of the $\chi\bar{\chi}$ system in $t\bar{t} + E_T^{\text{miss}}$ production for the DMF pseudoscalar model with $M_a = 100\,\text{GeV}$ (brown) and $M_a = 600\,\text{GeV}$ (magenta) compared to the 2HDM+a model with $M_a = 100\,\text{GeV}$, $M_H = M_A = M_{H^\pm} = 600\,\text{GeV}$, $\sin\theta = 0.7071$ and $\tan\beta = 1$ (cyan). Right: Acceptances of the two-lepton $t\bar{t} + E_T^{\text{miss}}$ analysis [?] as a function of $\tan\beta$. Shown are the predictions in the 2HDM+a model without (round black markers) and with the cut $m_{\chi\bar{\chi}} < 200\,\text{GeV}$ (square black markers), assuming $M_a = 150\,\text{GeV}$, $M_H = M_A = M_{H^\pm} = 600\,\text{GeV}$ and $\sin\theta = 0.35$. The DMF pseudoscalar model result (full black line) with its statistical uncertainty (dashed black lines) as well as the acceptance $\mathcal{A}_{\text{2HDM+a}}(M_a, M_A)$ (red triangles) as defined in (A.1) is also depicted. [Uli: Fix notation?]

following weighted average

$$\mathcal{A}_{\text{2HDM+a}}(M_a, M_A) = \frac{\mathcal{A}_{\text{DMF}}(M_a)\,\sigma_{a,\text{DMF}} + \mathcal{A}_{\text{DMF}}(M_A)\,\sigma_{A,\text{DMF}}}{\sigma_{a,\text{DMF}} + \sigma_{A,\text{DMF}}}\,. \tag{A.1}$$

In the right panel of Figure 32 we show the results that are obtained by applying the latter equation to a parton-level implementation of the two-lepton $t\bar{t} + E_T^{\text{miss}}$ analysis described in [?]. The round (square) black markers indicate the results of a direct calculation in the 2HDM+a model without a $m_{\chi\bar{\chi}}$ cut (imposing the cut $m_{\chi\bar{\chi}} < 200\,\text{GeV}$), using $M_a = 150\,\text{GeV}$, $M_H = M_A = M_{H^\pm} = 600\,\text{GeV}$ and $\sin\theta = 0.35$. The DMF pseudoscalar model result with its statistical uncertainty is represented by the solid and dashed black lines. The acceptance calculated from (A.1) is finally indicated by the red triangles. Two features are evident from the figure. First, the 2HDM+a acceptance with cut agrees with uncertainties with the acceptance of the DMF pseudoscalar model. This is expected because the cut $m_{\chi\bar{\chi}} < 200\,\text{GeV}$ strongly suppresses the A contribution in the 2HDM+a model. Second, the acceptance estimated using (A.1) agrees within uncertainties with the acceptance evaluated directly in the 2HDM+a sample.

Further validations of (A.1) are presented in Figure 33. In this figure we apply the rescaling formula to the case of the one-lepton [?] (left panel) and the hadronic [?] (right panel) final state arising in the context of $t\bar{t} + E_T^{\text{miss}}$ production. The direct 2HDM+a calculations are indicated by the black dots and error bars, while the grey and red (blue) bands illustrate the result in the DMF pseudoscalar model and the prediction obtained

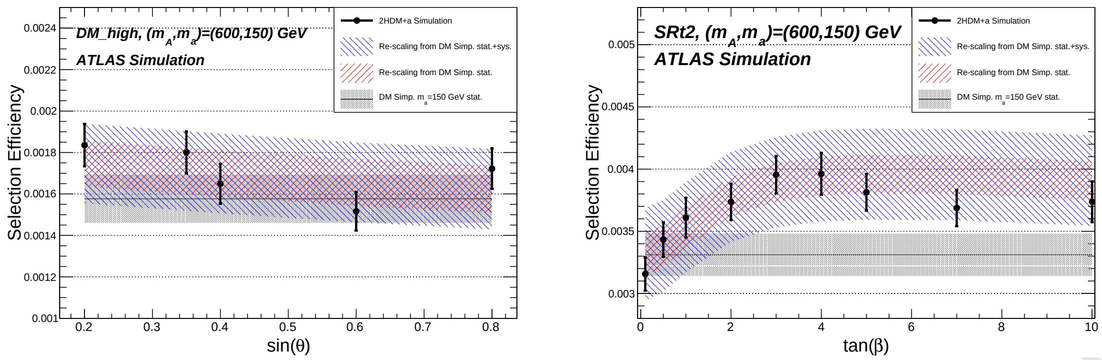

Figure 33: Validation of (A.1) in the case of the one-lepton (left panel) and the hadronic (right panel) final state arising from the $t\bar{t}+E_T^{\rm miss}$ signature. The direct 2HDM+a calculations are indicated by the black dots and error bars, while the grey and red bands indicate the result in the DMF pseudoscalar model and the prediction obtained using the rescaling formula. In the left (right) panel, the chosen parameters are $M_a = 150\,\text{GeV}$, $M_H = M_A = M_{H^\pm} = 600\,\text{GeV}$ and $\tan\beta = 1$ ($\sin\theta = 0.35$). [Fix notation?]

using (A.1) including statistical (statistical and systematic) uncertainties. In the left (right) panel, we have employed $M_a = 150\,\text{GeV}$, $M_H = M_A = M_{H^\pm} = 600\,\text{GeV}$ and $\tan\beta = 1$ ($\sin\theta = 0.35$). One observes that the rescaled results describe the $\sin\theta$ and $\tan\beta$ dependence of the 2HDM+a result well with uncertainties. We finally add that the formula (A.1) has also been successfully tested in the case that $|M_A - M_a| \simeq 50\,\text{GeV}$, in which case the interference between the a and A contributions is phenomenologically relevant.

B Distributions of the $t\bar{t} + E_T^{\rm miss}$ signal in the 2HDM+s model

In this appendix, we present a concise study of the kinematic features of the $t\bar{t} + E_T^{\rm miss}$ signature in the 2HDM+s model [? ?], focusing like in the case of the 2HDM+a model on the $E_T^{\rm miss}$ spectrum (for the related studies in the 2HDM+a model see Section 6.2). In Figure 34, we display normalised $E_T^{\rm miss}$ spectra corresponding to either the 2HDM+s model (coloured curves) or the DMF scalar model (black curves). In both panels the chosen parameters are $M_H = M_A = M_{H^\pm} = 600\,\text{GeV}$, $\sin\theta = 0.7071$, $m_\chi = 1\,\text{GeV}$ and $\tan\beta = 0.2$ as well as $\tan\beta = 1$, while in the left (right) plot we have employed $M_s = 100\,\text{GeV}$ ($M_s = 400\,\text{GeV}$). We observe that the shape of the 2HDM+s distributions always resembles the corresponding one of the DMF model within uncertainties. This feature is expected because in the considered parameter benchmarks the 2HDM non-SM Higgses are significantly heavier that the additional scalar mediator, and thus decouple. We add that by studying simple observables like $E_T^{\rm miss}$ it is in principle not possible to disentangle DM-scalar from DM-pseudoscalar interactions. Angular correlations between

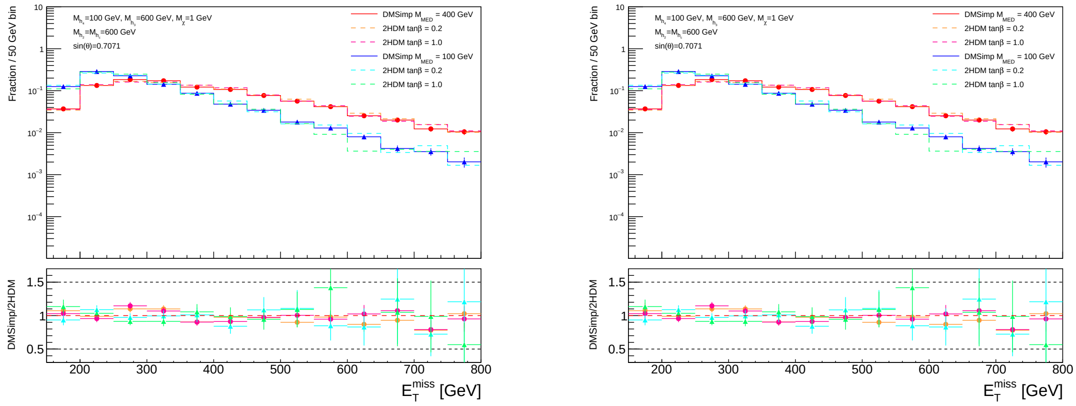

Figure 34: Normalised $E_T^{\rm miss}$ distributions for $t\bar{t} + E_T^{\rm miss}$ production in the 2HDM+s model. The black curves correspond to the prediction of the DMF scalar model, while the coloured predictions illustrate the results in the 2HDM+s model. In both panels the choices $M_H = M_A = M_{H^\pm} = 600\,{\rm GeV}$, $\sin\theta = 0.7071$, $m_\chi = 1\,{\rm GeV}$ and either $\tan\beta = 0.2$ or $\tan\beta = 1$ have been made. The mass of the scalar mediator s is set to $M_s = 100\,{\rm GeV}$ ($M_s = 400\,{\rm GeV}$) in the left (right) panel. [Uli: Make the two plots as described! Please make a linear-linear plot! Fix notation!]

two visible final state objects in $X + E_T^{\rm miss}$ events can however serves such a purpose [? ? ? ?].

C Details on the MC generation

The studies presented in this whitepaper are all based on MC simulations that use an `UFO` [?] implementation of the type-II 2HDM+a model as described in Section 3. The `UFO` implementation called Pseudoscalar_2HDM has been provided by the authors of [?] and a brief introduction to its basic usage can be found in README.txt. Below we give some details on the signal generation of the $t\bar{t}t\bar{t}$ channel discussed in Section 7 as well as the $h\,(b\bar{b}) + E_T^{\rm miss}$ and $Z\,(\ell^+\ell^-) + E_T^{\rm miss}$ signatures considered in Section 8.

Four-top signature

In Section 7 we have presented a study of the $t\bar{t}t\bar{t}$ channel, splitting the total four-top production cross section into three different contributions: one that only includes the SM graphs ($|{\rm SM}|^2$), another one that is due to new-physics only ($|{\rm NP}|^2$) and finally a contribution that accounts for both the SM and the 2HDM+a diagrams ($|{\rm SM} + {\rm NP}|^2$). In Table 1 we provide the `MadGraph5_aMC@NLO` syntax that has been used to generate the three different samples using the Pseudoscalar_2HDM `UFO`.

MadGraph5_aMC@NLO syntax	Legend symbol	Details
`p p > t t~ t t~ / a z h1 QED<=2`	$\lvert\mathrm{SM}+\mathrm{NP}\rvert^2$	Four-top production including both SM and NP contributions and their interference.
`p p > t t~ t t~ / a z h1 QCD<=2`	$\lvert\mathrm{NP}\rvert^2$	Four-top production from NP processes, including interference terms among H, A, a.
`p p > t t~ t t~ / a z h1 QED<=0`	$\lvert\mathrm{SM}\rvert^2$	Four-top production within the SM.

Table 1: MadGraph5_aMC@NLO syntax used to obtain the different curves shown in the two panels in Figure 19.

Mono-Higgs signature

The $h\,(b\bar{b}) + E_T^{\mathrm{miss}}$ sensitivity study presented in Section 8.1 is based on the generation of the signal using the Pseudoscalar_2HDM UFO together with MadGraph5_aMC@NLO and NNPDF23_lo_as_0130 parton distribution functions (PDFs) [?]. The MadGraph5_aMC@NLO syntax used to generate the gg-fusion contribution reads

```
import model Pseudoscalar_2HDM
g g > h1 xd xd~ [QCD]
```

where [QCD] indicates that one deals with a loop-induced process. The $b\bar{b}$-fusion channel is instead generated with

```
import model Pseudoscalar_2HDM-bbMET_5FS
p p > h1 xd xd~
```

The first command loads the version of Pseudoscalar_2HDM UFO corresponding to the five-flavour scheme (5FS). In this only the top quark is massive while the bottom quark is massless and thus can appear as a parton in the colliding protons. Both the top and bottom Yukawa coupling are however non-zero. [Uli: How has the decay been simulated?]

Mono-Z signature

The event samples that have been employed in the $Z\,(\ell^+\ell^-) + E_T^{\mathrm{miss}}$ sensitivity study (see Section 8.2) have been obtained using the Pseudoscalar_2HDM UFO in conjunction with MadGraph5_aMC@NLO, NNPDF30_lo_as_0130 PDFs [?] and PYTHIA 8.2 [?] for parton showering. The MadGraph5_aMC@NLO syntax used to generate the samples is

```
import model Pseudoscalar_2HDM
g g > l+ l- xd xd~ / h1 [QCD]
```

where $l = e$ or μ and only contributions from gg-fusion have been considered. To increase the efficiency of the event generation, Feynman diagrams with an intermediate s-channel SM Higgs boson have been explicitly rejected using the `MadGraph5_aMC@NLO` syntax `/ h1`.